coatings

MDPI

Review

Advancements in Electrospark Deposition (ESD) Technique: A Short Review

Claudia Barile, Caterina Casavola, Giovanni Pappalettera and Gilda Renna *

Dipartimento di Meccanica, Matematica e Management, Via Orabona 4, 70125 Bari, Italy
* Correspondence: gilda.renna@poliba.it

Abstract: The need to use components with improved surface characteristics in relation to severe operating conditions, together with the aim of cost reduction associated with the replacement of damaged components, has led to an increasing use of coatings and repairing processes. The most common deposition processes are generally characterized by high equipment costs and, sometimes, by long deposition time. Furthermore, some repair technologies, especially those characterized by high heat input, are not suitable for alloys used in aerospace applications due to the degradation of their mechanical characteristics. In the last decades, a novel eco-friendly method capable of overcoming the limits set out above emerged: the electrospark deposition (ESD) technology. Thanks to its efficiency, simplicity, cost-effectiveness, and low heat input, this technology has proved to be suitable both for improving surface properties, such as thermo and wear resistance, higher hardness and corrosion resistance, and for the repair of high-value components. The aim of this review is to describe in detail some aspects of the ESD technique to understand the ESD processing preparation of alloys normally considered difficult to weld by traditional processes and to give some important clues to the readers to contribute to the defect-free repair of damaged areas and coatings deposition.

Keywords: electrospark deposition; ESD; coating technology; repairing; worn metal components; pulse fusion surfacing; spark hardening; spark toughening; metal substrates

Citation: Barile, C.; Casavola, C.; Pappalettera, G.; Renna, G. Advancements in Electrospark Deposition (ESD) Technique: A Short Review. *Coatings* **2022**, *12*, 1536. https://doi.org/10.3390/coatings12101536

Academic Editor: Salvatore Grasso

Received: 19 July 2022
Accepted: 8 October 2022
Published: 13 October 2022

1. Introduction

Protection and repair have a very important role on the modern technology in industry. Coatings are considered the backbone for advanced applications in various fields, for example, gas and steam turbine blades, and in the metal-working, medical, military, recreational equipment applications and so on. Over the past decades, the coating and repair procedures that can be performed in situ and, at the same time, can take into account demands for energy saving and sustainability have gained increasing interest, especially in the aerospace and aeronautic sectors [1–3].

Nowadays, many kinds of surface treatment technologies (i.e., electroplating, physical vapor deposition, thermal diffusion, and chemical vapor deposition) used to improve the anti-softening, wear and corrosion properties of component material are not suitable. The crucial issues for all coating and repair applications depend on the high pollution, cost of equipment, and long processing time [4–7]. Besides, a main issue is the high heat input into the workpiece, resulting in thermal distortion and/or changes in the metallurgical structure of the substrate (heat-affected zone (HAZ)) [7]. Very often, the microstructural and physical characteristics of the alloy prevent the use the fusion welding repair techniques (i.e., tungsten inert gas welding (TIG), laser, electron beam, or an equivalent process) [7–13]. For example, the fusion welding repair processes of components that are made of Al alloy or Ni superalloys are not suitable because these alloys are particularly prone to cracks during the solidification period, both in the welded (i.e., hot cracking) and in the base metal (i.e., liquation cracking) [14–17].

The outstanding versatility and special capabilities of the electrospark deposition (ESD) process have been recognized in the 21st-century technology, a time in which many

researches have pointed out as this low-heat-input processes has great potential for coatings application and restoration of damaged high valued parts [18–21].

ESD is a low-heat-input pulsed micro-bonding process that uses short-duration, high-current electrical pulses to weld a consumable electrode material to a metallic substrate. This process is analogous to a pulsed micro-arc welding process, but it differs from this in that it uses electrical pulses typically three orders of magnitude shorter [22–26].

When the energy stored in a capacitor bank is discharged, the electric current pulse generates a plasma arc for a short time (typically, 1–10 μs) between the tip of the electrode (anode) and the substrate (cathode), having a maximum arc temperature reaching 5000–25,000 K depending on the nature of the shielding gas used and the current conducted by the plasma [26,27]. The electric arc generated is able to melt and vaporize a small material volume fraction of both the substrate and the electrode. The small molten droplets from the electrode are propelled and accelerated by the electric field towards the substrate, where they crash, producing a deposit with strong adhesion. Pulse durations of a few microseconds and pulse frequencies in the 0.1 to 2 kHz range, associated with a small amount of transferred material, allow substrate heat dissipation over 99% of the duty cycle. Since the heat input to the substrate is low (heating only 1%), the average temperatures are generally below 80 °C [26–30]. Thanks to the low heat input, the process does not produce significant distortions, shrinkages, and high thermal stresses, and above all, it eliminates or reduces the HAZ (highly undesirable zone) down to a few micrometers [29–33]. Therefore, ESD is particularly suitable for the treatment of thin or heat-sensitive metal substrates (i.e., MCrAlY and 2000 Al alloys) [20,21,29,34]. Furthermore, the high cooling rates involved lead to the formation of advanced microstructures: nanocrystalline or amorphous structures [30,35,36]. Additional advantages of this process include pollution-free, technological ease of depositing a metal under normal atmospheric conditions, cost-effectiveness of equipment, and portability of the ESD machine for use directly on the field (for example, shop). Furthermore, the ESD process can be manual or automated. Generally, manual application is often used to quickly coat component surfaces on which quality check and reproducibility are not required. The automation of this process, on the other hand, has proved to be a necessary requirement for obtaining reproducible coatings [24,31,33,37,38].

ESD applications range from treating cutting tools and machine components, often with tungsten carbide or titanium carbide–based electrodes, to repairing wear damages in steam generator tubes, gas turbine parts used in the aeronautical and automotive industry, engine components, pump components and so on [32]. To date, ESD is used to deposit a wide variety of combinations of electrically conductive electrode and substrate materials [20,22–26,39,40]. Researchers have demonstrated the ability of ESD to form a strong metallurgical bond of the coating to the substrate using electrodes of both homologous and dissimilar material from the substrate. Liu et al. [40], as well as Cadney and coworkers [41,42], demonstrated the possibility of depositing, by means of the ESD technology, both amorphous and crystalline electrodes on an amorphous substrate without obtaining its recrystallization. Similarly, Xie and Wang [23] showed that this process is able to produce a high-quality NiCoCrAlYTa coating, consisting of a uniform superfine columnar microstructure. Meanwhile, Hasanabadi et al. [43] examined the electrospark coating microstructure of as-cast $Fe_{48}Cr_{18}Mo_7B_{16}C_4Nb_7$ crystalline alloy deposited on a 316L stainless steel substrate. A. N. Sheveyko et al. [44] showed the possibility of depositing thick (up to 30 μm) and rough (average surface roughness greater than 6 μm) multicomponent TiCaPCO(N)-(Ag) coatings on titanium substrates by pulsed ESD in different environments (i.e., deionized water, argon, and air) using TiC-CaO$Ti_3PO_{(x)}$ and TiC-CaO-$Ti_3PO_{(x)}$-Ag_2Ca electrodes produced by self-propagating high-temperature synthesis.

Some studies have aimed at understanding the basic principles of ESD, and they have led to the development of the process and, consequently, to an increase in potential applications [45]. Several scholars have studied the mass transfer mechanism in the electrospark technology in detail [46,47]. Especially, Gallinov and Luban [48] have presented a method capable of determining the efficiency of mass transfer. This method, also known as the

transfer coefficient, is based on the constant monitoring of the erosion of the anode and the mass gain of the cathode.

Other studies have analyzed both the influence of ESD process parameters on the development of the microstructure and the properties of the coatings, as well as the defects of coatings deposited onto a similar or dissimilar metallic substrate [20,49–51].

This review article presents a comprehensive overview of the ESD process used for the deposition of both corrosion and wear-resistant coatings and for the restoration and refurbishment of worn or damaged areas. Furthermore, to better understand ESD technique deposition, in the first sections, the intrinsic aspects and the most reliable theories on the deposition mechanism of electrospark and the influence of the main process parameters on the efficiency of deposition are presented and discussed.

2. Electrospark Deposition (ESD) Technique

2.1. Background of ESD Technique

ESD is not a recent technology. The first uses of this technique aimed to create hard and resistant coating surfaces through processes such as pulse fusion alloying, spark hardening, pulse fusion surfacing, and electrospark alloying [52].

Rawdon was the first to experience the spark deposition phenomenon in 1924 [52,53]. In particular, Rawdon achieved a significant hardening of the pure Fe substrate by sparking a homologous material electrode, leading to martensite formation. For such a carbon-free Fe material, this was indeed a very important achievement. Therefore, martensite formation is due to the fast quenching of the small volumes of Fe, which undergo a very fast melting/freezing cycle. This is nothing more than a form of rapid solidification.

In 1957, Welsh [54] showed that extremely hard surfaces can be obtained on steel by sparking it with electrodes of WC (tungsten carbide) and W/TiC (titanium carbide). In addition, it demonstrated the feasibility of hardening the surfaces of copper, brasses, aluminum, and titanium using this technology [54–56]. The fact that such a relatively simple process can produce marked improvements in the wear resistance of different materials has attracted the attention of numerous researchers. Several investigations on spark deposition conducted by ESA researchers in the Soviet Union, between 1948 and 1999, led to the development of corrosion- and wear-resistant coatings for coal gasification apparatus, high-performance coatings on nuclear reactor components, and major enhancements in equipment for the deposition of sparks [32,56–60]. Over the past decades, even in the United States, research and development on ESD have been obtained, thanks to the strong interest from large private companies, such as General Electric, Pratt and Whitney, Rolls Royce Corporation, Aircraft Engines, General Electric Power Systems, and Advanced Surfaces and Processes.

Further improvements in the ESD equipment have led to the use of this technology not only to deposit coatings on nuclear reactor components, but also to deposit anti-wear and anticorrosion coatings on mechanical components subjected to strong thermal and dynamic stresses in the energy, aeronautic, and automotive sectors [61].

2.2. Principle and Apparatus of ESD

The electrospark deposition equipment is essentially composed of two main components: a capacitor-based power supply and an electrode holder (also known as applicator or torch) [27,62]. The most common power supply consists of a current rectifier, which transforms alternating current into direct current (DC) needed to charge up a series of capacitors and the discharge circuit. To discharge the capacitors, the power supply uses a resistor–capacitor (RC) or a microprocessor-controlled discharging circuit [27,62]. The electrode, controlled by the torch, is connected to the positive pole of the capacitance bank, while the workpiece (substrate) is connected to the negative one [32,52,62]. The electrical circuit between the electrode and the workpiece is completed by an electrical ground cable fixed to the workpiece [27]. Figure 1 shows the equipment for the electrospark deposition. Moreover, an inert gas supply system is added to the electrode holder to allow a cover

gas to flow over the deposition site at all times. Generally, the shielding gases used are: argon, helium, carbon dioxide, and mixtures of these gases. The inert gas protects the deposited metal from oxidation, provides cooling, and affects the physical properties of the arc, thereby also affecting the characteristics of the deposit [62].

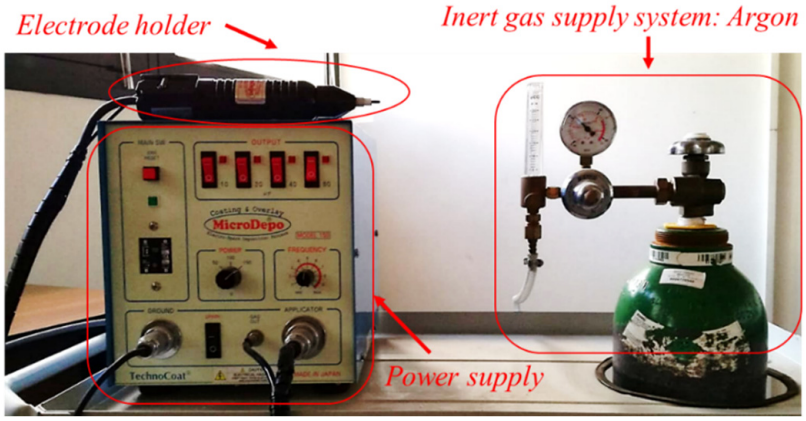

Figure 1. Electrospark deposition apparatus.

The electrode is in continuous relative movement against the substrate, by rotation or vibration. The relative motion of the electrode is necessary to avoid welding with the substrate, on which the coating or deposition is carried out. When the rotating consumable electrode is subsequently in mobile contact with the substrate (short circuit), the energy stored in a capacitor bank is discharged through a sequence of short electric sparks at low voltage and high current. Following the electric discharges, the metal is transferred, from the electrode to the substrate, through the emission of melted droplets that occur in micron gaps filled with a dielectric gas [26,27,63]. Unfortunately, the ESD technique has been found to suffer from serious deficiencies in process stability, resulting in coating discontinuity spatter layers, crater erosion, and high surface roughness. In general, a variety of effects may contribute to the process instability. Most notably, the process instability can be attributed to the nature of the dielectric gas, which has been recognized to heavily affect the mass transfer mechanisms and the surface coating topography. In particular, it was found that in depositions, in the absence of shielding gas, the size of the molten droplets increases, giving rise to a very uneven deposition. The larger size of the droplets is due to the fact that the high thermal conductivity plasma generated by molecular gases (i.e., nitrogen and oxygen) promotes a globular/spray-type mass transfer mechanism [26,63]. Unlike the depositions carried out in the air, those carried out in the presence of Ar shielding gas lead to finer spray depositions and more uniform surfaces, thanks to the formation of smaller droplets compared with those generated in the presence of air. However, many other factors influence the stability of the deposition process. First of all, the process instability can be linked to an irregular geometry of the contact surface in the discharge zone. In the literature, it is reported that these irregular contact surfaces are generated both by a change of the electrode and by the discharge conditions, such as due to a change in the shape of the electrode tip or in the roughness of the coating, respectively. Moreover, very often, very harmful transient arcs are established due to these irregular contacts, leading to a high transfer of energy and overheating of the electrodes and spot localization. Again, the process instability may also be attributed to the inhomogeneity of the electric field, which can lead, depending on the intensity, to partial or total discharge phenomena [26,64,65].

As shown by Frangini et al. [26], the spark discharge is generally not a stationary process but, in reality, only a transition mechanism characterized by a voltage activation peak, which, if the short-circuit current will not be disrupted, ends unequivocally with a stationary thermal arc (Figure 2). Moreover, the local oscillations of the electric field are caused by the irregularity of the microgap space generated during the relative movement of the electrode along the substrate. A variation of the microgap space during the deposition

generates a great variability of the activation peak of the voltage and the energy available for the discharge pulses, thus being the cause of uneven deposition.

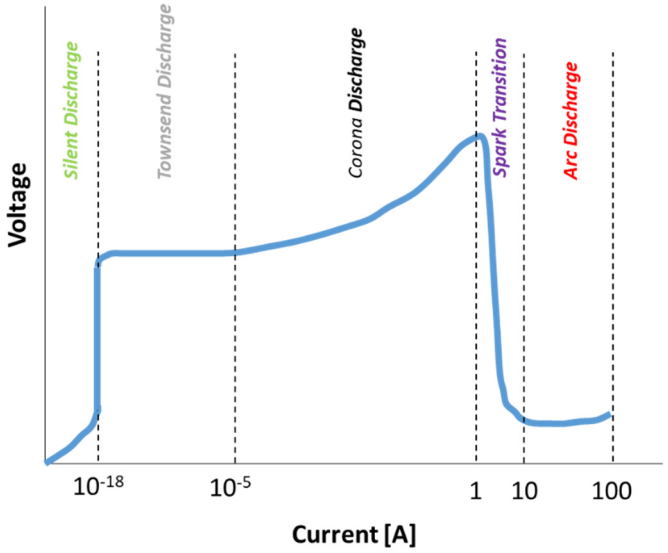

Figure 2. Representation of tension–current behavior of stationary electrical discharge in gas at atmospheric pressure [26].

2.3. ESD Parameters

A variety of process variables can contribute to the properties and quality of the deposits. These may include mechanical and electrical parameters. The mechanical parameters include rotation and/or oscillation velocity of the electrode, travel motion of the electrode along the substrate, step-over at each pass to allow some overlap of the deposit, and electrode contact force against the substrate. Instead, electrical process parameters include capacitance, discharge frequency, charging voltage, pulse current and circuit inductance, and pulse duration (waveform width), which are directly controlled by the power supply [52]. In particular, the voltage, current, and capacitance are those variables that greatly affect the deposition quality as they affect the spark energy *Ep*, defined as:

$$Ep = \int_0^{tp} V(t) * I(t)dt \quad (1)$$

where *tp* is the pulse duration and $V(t)$ and $I(t)$ are a function of the voltage and of current during discharge, respectively [32,66]. By multiplying the capacitance by the voltage, it is possible to calculate the pulse-energy *Ep*:

$$Ep = \frac{1}{2}nCV^2 \quad (2)$$

where *Ep* is the pulse energy, *n* is the fraction of capacitor discharge that occurs during arcing, and *V* and *C* are the voltage and the capacitance, respectively [32,66].

Therefore, the use of higher voltages and currents leads to an increase in the deposition rate and roughness. More specifically, a higher capacitance produces a wider pulse width. Therefore, the greater the capacitance, the greater the duration of the discharge for a given voltage potential. By changing the capacitance and the voltage, the duration of the discharge and the peak current are altered, respectively. Instead, the charging voltage (V) controls the amount of the current flowing through the capacitor.

The spark duration of the ESD process is usually limited to a few microseconds. Compared with other arc welding processes, the spark duration of the ESD process is generally about three orders of magnitude shorter. Moreover, it is possible to change the deposition frequency from 60 to 4 kHz [52,62,66,67].

Detailed studies on the ESD technique have shown that discharge parameters (such as frequency, voltage, and capacitance) depend on the melting temperature of the electrode and the type, electrical resistance, chemical reactivity of the anode elements, thermal conductivity, density, diffusivity, flowability, and thermal inertia. Moreover, it was found that the base material influences the electric parameters by its melting point, conductivity, boiling point, and affinity absorption for discharge gases [45,68]. Other key factors are: number of passes, amount of overlap between passes, and spark time per unit area. In Table 1, all the important process parameters affecting the quality and properties of the resultant deposition are summarized.

Table 1. Summary of ESD process parameters. Adapted from [52].

Substrate	Electrode	Electrical	Protective Environment	Other
Material	Material	Power input	Shielding gas type	System efficiency
Surface	Geometry	Voltage	Flow rate	Number of passes
Finish	Motion	Capacitance	Temperature	Overlap of passes
Cleanliness	Speed	Spark rate	Flow geometry	Spark duration
Temperature	Contact pressure	-	-	-
Geometry	Orientation	-	-	-
-	Application direction	-	-	-

2.4. Materials: Base Material and Electrode Materials

The substrate and electrode materials suitable for this process are all those electrically conductive materials, that is, all those materials that are melted by means of an arc [62,66,67,69]. To date, several types of metals and ceramic/metal deposits are manufactured by ESD [26,39], including superalloys [22–24], Mg alloys [25], iron-based alloys [40], and so on [20]. The most commonly used electrode materials are those applied to produce wear resistance and corrosion resistance coatings (i.e., hard alloys, carbides, borides, intermetallics or cermets), followed by those that improve the corrosion or oxidation resistance of the surface, while the least used are refractory metals and structural materials. Figure 3 summarizes the applied coatings and alloys of ESD-coated substrates to date. Moreover, the ESD process is able to bond dissimilar materials that are incompatible with traditional welding techniques. However, it is recommended in the literature to use electrode materials that have a lower hardness than the substrate material to avoid abrasive wear during deposition. In other words, when the electrode has a higher hardness than that of the substrate, the inverse phenomenon of deposition occurs: electroerosion [32].

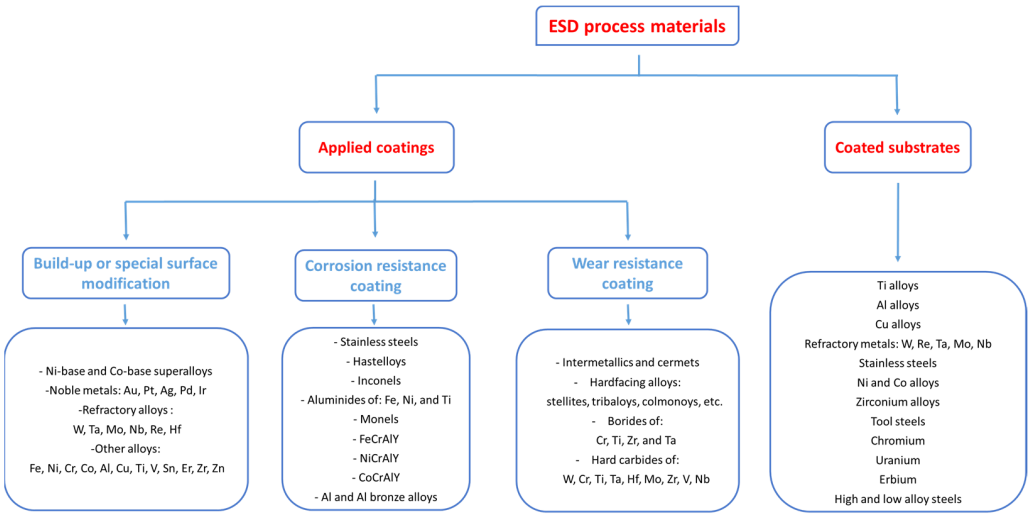

Figure 3. Chart of applied coatings and alloys of ESD-coated substrates to date. Adapted from [70].

2.5. Mechanism of Building Deposited Layer in ESD: Material Transfer between Deposit and Substrate

Over the years, many researchers have advanced different hypotheses on the material transfer mechanism from the rotating electrode to the substrate during the electrospark process [48,67,71]. However, the heuristic physical model proposed by Liu et al. [69] to explain the mechanism of the transferred material was the most widely accepted. Figure 4 shows the scheme of the proposed physical model. In this model, the process is divided into four stages. Initially, the rotating electrode is shifted until the tip touches the substrate locally (1° stage, Figure 4a). Immediately after (2° stage), a pulsed electrostatic discharge is generated between the electrode tip and the substrate. The large amount of energy and current provided by the discharge rapidly leads to the melting and gasification of both the electrode material and a small amount of the substrate material. In particular, at this second stage, there is the generation of a melted pool on the substrate and small melted droplets of electrode material (Figure 4b). Furthermore, it has been found that the heat input is able to improve the ionization of the gas present between the substrate and the rotating electrode. High temperatures and pressures are generated in the contact microzone (Figure 4b,c). Subsequently, thanks to the rotation of the electrode, the melted drop formed is rapidly propelled towards the melting pool; here, it impinges on the substrate and solidifies rapidly (Figure 4c) [19,69]. Due to the small melt thickness and the high heat transfer rate among the substrate and the melt, or even the previous deposit, it can be assumed that the temperature gradient, the solidification rate, and the cooling rate are constant at all times inside the single deposit and perpendicular to the surface of the substrate [24]. At the end in the fourth stage, a new discharge cycle will take place as the substrate and electrode come into contact again (Figure 4d).

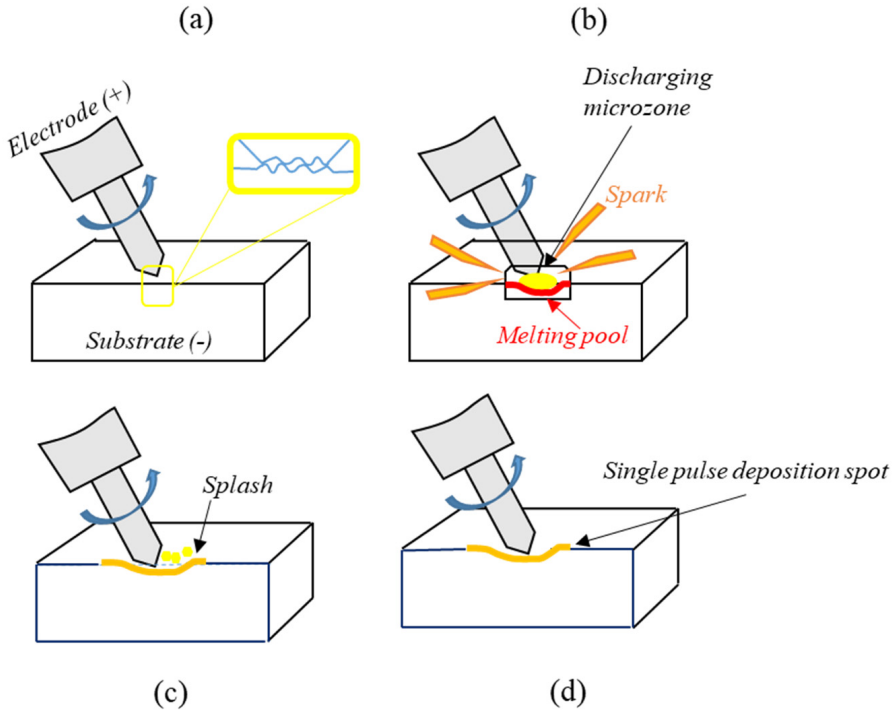

Figure 4. Schematic diagram of the material transfer mechanism in the rotating ESD process: (**a**) 1° stage, the electrode is moved until the tip touches the substrate locally, (**b**) 2° stage, a pulsed electrostatic discharge is generated between the electrode tip and the substrate; the large amount of energy supplied leads to the formation of fused droplets of electrode material and a small amount of substrate material, (**c**) 3° stage, the molten droplet is rapidly rushed to the melt pool impinging on the substrate and solidifying, and (**d**) 4° stage, the electrode and substrate will contact again and a new discharging cycle is started. Adapted from [69].

A study by Thamer A. D. et al. [39] shows that the deposit surface is characterized by three morphologically different regions (Figure 5a). The first is called "near region", and it is the region that originates on both sides of the track from the weld. This region appears as a white area because, in addition to the drop of molten metal, the vapors released by the fusion are also deposited (Figure 5b). Region 2 does not necessarily occur in all electrospark processes but only in some cases and based on the displacement of the electrode with respect to the substrate (Figure 5c). This is an intermediate and nonuniform region. Moreover, in this region, it is possible to see and count all the passages performed by the electrode [39]. Generally, when the deposition is performed manually, it is difficult to calculate the overlap percentage, as this depends on the movement speed of the electrode. Moreover, it was found that if the discharge frequency is very low and the electrode follows a linear movement, an inadequate overlap of the splats occurs, resulting in high porosity, increased chance of microcracks, and therefore weakness of the deposit [39,45]. Conversely, the increasing overlap leads to increased temperature locally and can create HAZ, leading to microcracks in the substrate alloy and can also create global separate asperities, leading to a rough surface. The third region is defined as the main area and is characterized by low porosity. Unlike region 2, in this region, it is difficult to identify the splashes of the microdrops [39].

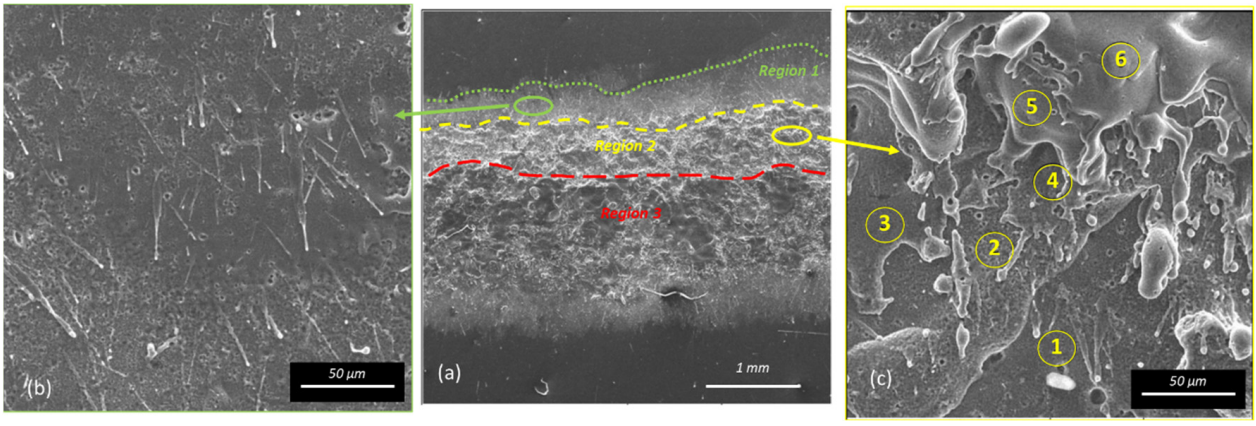

Figure 5. (**a**) SEM micrograph showing the deposition track of NI6625 (Inconel 625) upon Inconel 738 substrate with variables of 25 volt, 400 Hz, and rotating electrode of 600 rpm using argon; (**b**) SEM micrograph of region 1 at higher magnification showing the splashes produced by the impact of the drops following the direction imposed by the electric discharge; and (**c**) SEM micrograph of the deposition in region 2 at higher magnification showing the six overlapping layers. Adapted from [39].

Figure 6 shows the representative drawing of the single spark effect on the cross section during the movement of the electrode towards the left and what happens when a second drop is generated. The heat produced by the discharge of the electric spark evaporates and expands a small amount of material, causing a very high local pressure; consequently, the liquid pool will splash into the surrounding and solidify due to the heat absorbed by the lower substrate (Figure 6a). It is noteworthy that at the point where the electrode material is mixed with the base material, the surface takes the form of a forward bent arc (region 3). At the same time, some drops will tend to fly away and impact in more distant areas together with the vapors, thus creating region 1 (Figure 6a). When the second electrical discharge occurs, the heat produced generates evaporation and melts the previously deposited material together with a small amount of substrate, bonding with the new molten electrode material, which is diluted from the old deposited layer. Therefore, the new material contains about 60% of the electrode and 40% of the prior deposited layer (see the green area in the drawing, Figure 6b). Figure 6b shows how the advancement of the electrode determines the geometry of the subsequent deposits [39].

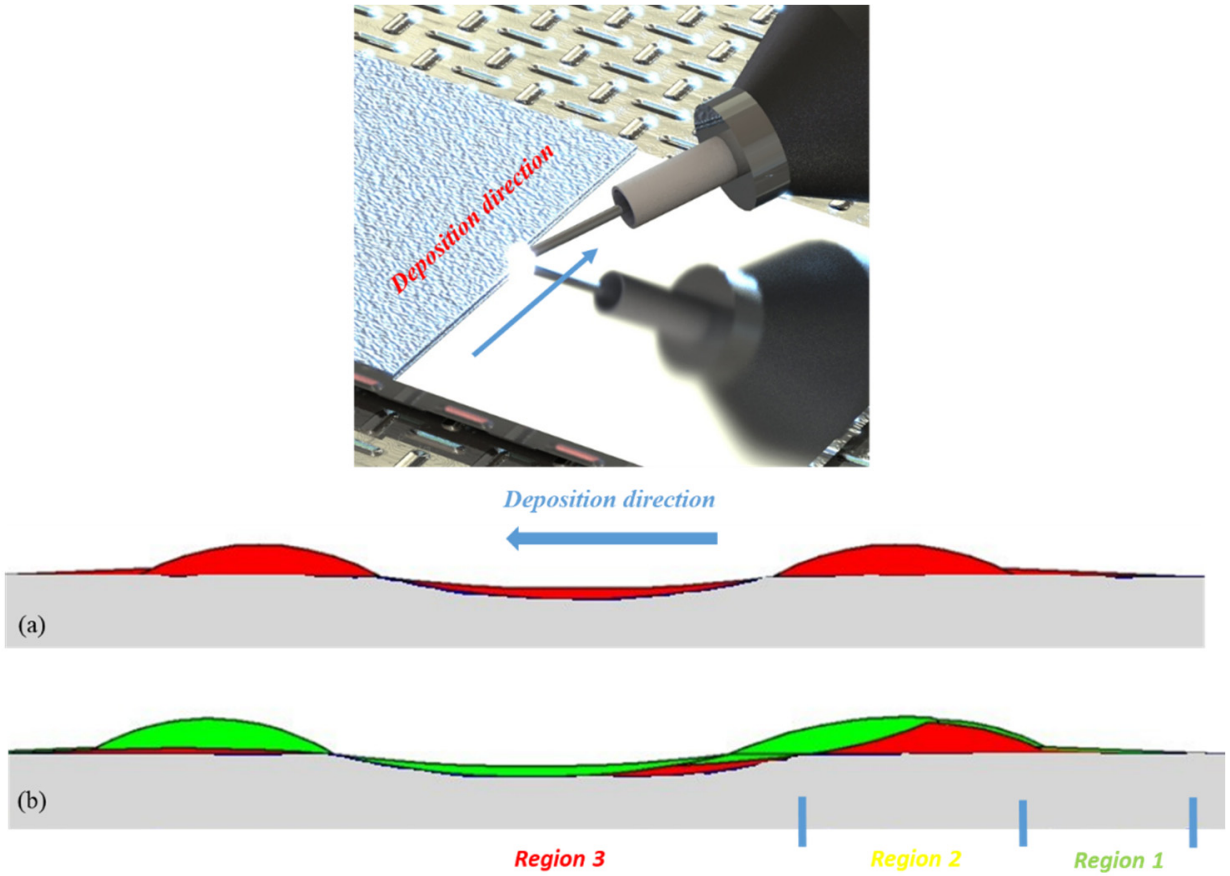

Figure 6. Schematic representation of the distribution of the resulting material (**a**) to the single spark and (**b**) with a second overlapped spark. The substrate is represented in gray, the formation of the first splat in red, and the formation of the second splat in green [39].

2.6. Microstructure Morphology of Electrospark Coatings

The high cooling rates (about 10^5–10^6 °K/s) involved during the electrospark deposition process determine the formation of advanced microstructures during solidification [40,43,67]. More specifically, the solidification microstructure of a specific alloy is directly correlated with the solidification conditions predominant at the transformation front. Specifically, the temperature gradient G (K/m) at the solid/liquid interface and the solidification rate (or also called growth rate) R (m/s) are the fundamental quantities that determine the solidification structure [20,72]. The morphology of the solidification microstructure is determined by the G/R ratio [20,23]. In particular, low values of this ratio imply an equiaxial dendritic growth, while very high G/R values lead to cellular dendritic or cellular growth up to even having a planar growth. Consequently, the lower this ratio, the greater the tendency towards the growth of equiaxial dendrites.

Instead, the scale of the solidification structure is determined by the product G × R. This product is named with T corresponds to the cooling rate. Therefore, higher cooling rates imply finer microstructures. Often, the microstructure sizes may not be the same at several points of the deposition [20]. In general, the microstructure scale in electrospark deposition is always very fine as the process generates splats characterized by a very small volume of molten metal during each pulse. When splats come into contact with the cold substrate, they undergo very high cooling rates. Figure 7 represents schematically the various solidification morphologies and how these depend on R and G.

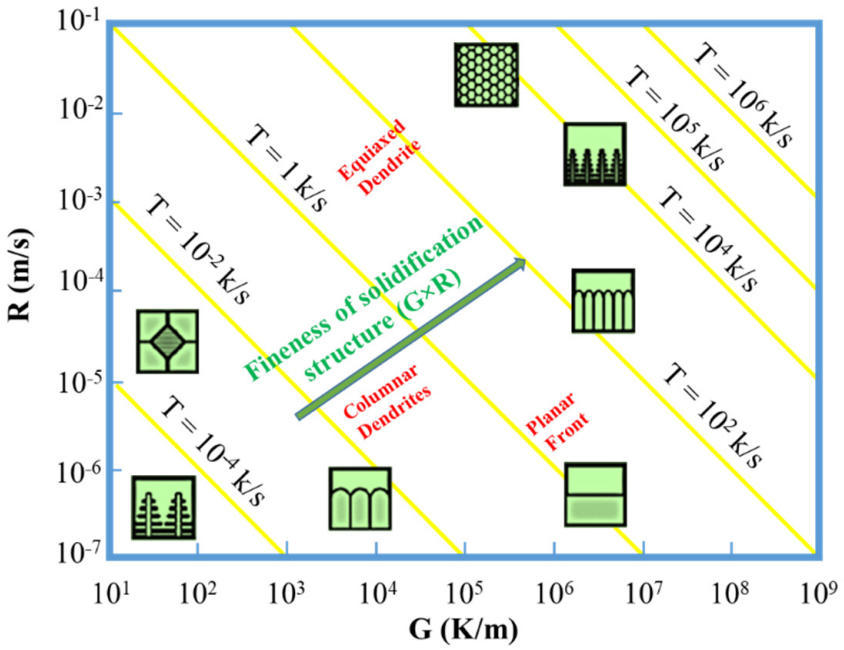

Figure 7. Schematic representation of the influence of the solidification rate (R) and the temperature gradient (G) on the final morphology of the microstructure [24].

When G is the predominant factor, there will be a development of a planar morphology. Under these conditions, it will be possible to obtain a chemically homogeneous solidified material, thanks to a low tendency to solute or chemical segregation. Meanwhile, as R begins to increase, a solute gradient begins to develop, and planar morphology gives way to a cellular structure. Finally, a dendritic solidification morphology and greater chemical segregation is obtained when R is the predominate factor [24].

2.7. ESD for Coating Purposes

Thanks to the wide variety of materials that the ESD process can deposit, this process finds several kinds of applications for which it can be used as a surface engineering process. Specifically, the applications receiving electrospark deposition treatments are principally of two types: restoration and refurbishment of worn or damaged components (repair) and coating deposit. Generally, coating deposit application consists in the enhancement of the tribological and corrosion properties of surfaces especially in relation to the rapid solidification event that leads to the microstructure refinement at the nanostructured (nanocrystalline structures) or amorphous levels.

2.7.1. Nanocrystalline Deposits

It is known that nanostructured materials, in general, show improved toughness, enhanced diffusivity, increased strength/hardness, reduced elastic modulus and ductility, enhanced CTE (thermal expansion coefficient), and higher specific heat than conventional materials [73]. For that reason, it is important for the manufacturing industry to acquire the ability to fabricate nanostructured deposits using eco-friendly and low-cost processes. Deposits with a nanocrystalline microstructure have been the object of many studies over the past couple of decades with considerable progress in their understanding especially in recent years. The nanocrystalline structures, also known as "ultrafine grain size structures" are single- or multiphase polycrystals with nanoscale (250–1000 nm) grain size. In other words, nanocrystalline deposits are structurally characterized by a large fraction in the volume of grain boundaries (interfaces) inside which a substantial fraction of atoms lies [73].

In the literature, several studies show the ability of the electrospark technology to obtain a material coating with a highly refined microstructure by depositing both homolo-

gous and dissimilar electrode materials to the substrate. For example, Figure 8a–d shows the morphology and microstructural changes that occur in Al-based alloy coatings as a consequence of rapid solidification [20,30,33]. It is worthy of note that coatings consist of many superimposed thin layers. The layered structure is depicted in Figure 8a, where both some layer–layer interfaces and one single deposited layer are also indicated by arrows. The subsequent superimposed layers and the first one to be deposited on the substrate are bonded by metallurgical reaction, such as diffusion or fusion [11,20]. As it can be observed in Figure 8b,c, the most frequent morphologies related to the ESD process are equiaxed dendritic or cellular dendrite morphology. Specifically, the layer–layer interfaces are generally characterized by the presence of equiaxed dendrites (indicated by the arrow B in Figure 8b), while the different layers are characterized by the presence of a cellular dendritic microstructure (indicated by arrow A in Figure 8b). Generally, the microstructural morphology and scale within the coating are nonuniform but highly variable due to the different local solidification conditions induced by the deposition process. A study on high gamma prime superalloy IN-792 coating deposited showed that the typical cellular microstructure grows antiparallel to the heat flux direction [24]. In addition, Y. Xie et al. pointed out that in the deposited layers, grains grow vertically passing through layers and form long columnar grains with a preferential growth orientation along the buildup direction [24].

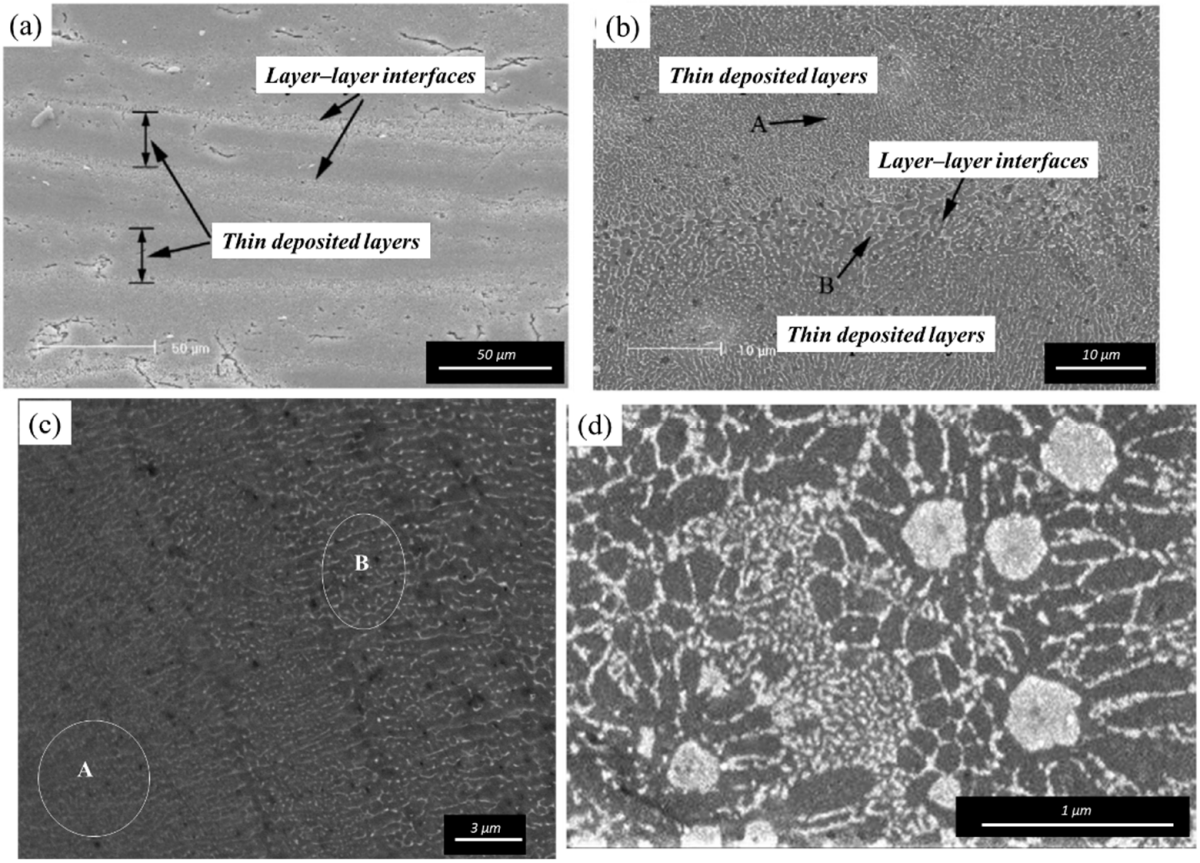

Figure 8. Microstructural morphology in the Al-based coatings: (**a**) structure of Al–Si coating deposited on ZL101 Al alloy substrate [33], (**b**) magnification of Al–Si coating deposited on ZL101 Al alloy substrate showing the microstructures to the layer–layer interface and of two thin deposited layers [33], (**c**) microstructure of Al 2024-T4 coating deposited upon homologue substrate (the circles A and B point out the same cellular dendritic microstructure more or less fine in different layers) [20], and (**d**) microstructure of Al-17Si alloy coating [30].

M. Brochu et al. [30] showed that ESD can be easily used to considerably refine the microstructure of the Al–17Si electrode material. The microstructure of the Al-17Si deposited material is depicted in Figure 8d. In particular, compared with the average primary Si particle size in the cast electrode (60 ± 37 μm), they found that after deposition, the primary Si particle size was reduced by two orders of magnitude to 256 ± 68 nm. Generally, Al–Si coatings consisting of a fine dispersion of particles of spherical morphology are strongly desired since this morphology reduces the tendency towards microcracking and particle pullout [30,74,75]. At the same time, the spherical phase of fine Si distributed throughout the aluminum matrix gives excellent performance and greater wear resistance to Al–Si coating [76]. Instead, W. Wang [33] showed that the Al–Si coating fabricated by electrospark deposition exhibits greatly superior cavitation erosion resistance than the cast Al–Si alloy substrate.

Furthermore, it is well known that coatings/components characterized by the presence of an intermetallic phase of small size are characterized by better mechanical properties due to an increase in the impact of the dislocation movement in relation to the greater surface between the intermetallic and the matrix. Based on this, many scholars have investigated the possibility of producing deposits displaying a high refined intermetallic phase using the ESD process. Heard et al. [77] claimed that the optimal pulse energy required for refining the Al_3Ni intermetallic within a hypoeutectic Al–Al_3Ni alloy at the nanoscale was 0.1 J (100 V and 20 F). However, using this energy value, the particle size of the Al phase was ~25 nm. The minimum grain size of Al can be calculated from X-ray diffraction spectra by Scherrer's equation:

$$t = \frac{0.9\lambda}{B\ cos\theta} \quad (3)$$

where t is the crystallite size, λ is the radiation wavelength (Cu Kα = 1.54 Å), B is the full width at half maximum (FWHM), and θ is the angle in radians. Meanwhile, due to the overlapping of nearby peaks, the minimum grain size of the Al_3Ni phase was calculated with the SEM analysis, and the results were ~44 nm [77]. The XRD spectra of the for-Al–Ni alloy deposit and the as-cast ingot used to produce the electrode and the SEM micrograph used for the determination of the minimum grain size of the Al_3Ni phase are shown in Figure 9a,b, respectively [77]. A similar conclusion was reported by Zhang [78]; in addition, the authors pointed out that decreasing the size of the Al_3Ni precipitate within an Al–Al_3Ni eutectic alloy leads to a notable improvement in the pitting corrosion resistance.

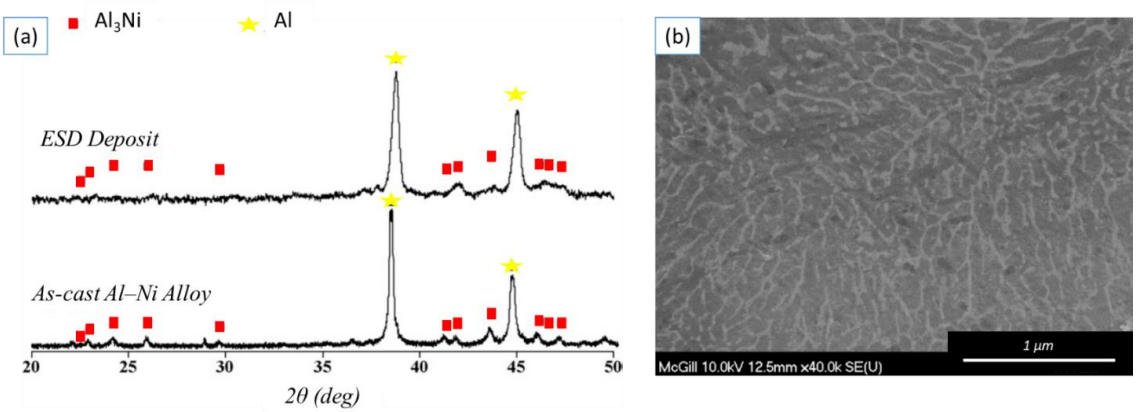

Figure 9. (**a**) Comparison between the X-ray diffraction spectra of the ESD deposit and the as-cast ingot for Al–Ni alloy and (**b**) SEM micrograph of an Al–Ni coating produced using a pulse energy of 0.1 J [77].

Wang Mao-cai et al. [79] investigated using SEM and TEM the microstructural characteristics of a NiCoCrAlYTa coating epitaxially built-up on a directionally solidified (DS) Ni-based superalloy blade tip by ESD. They showed that the coating consists of the overlap of several layers. In particular, the built-up coating exhibits zones characterized by the

presence of microstructures, such as cellular dendrites and very fine columnar dendrites and transition zones. More specifically, the layer consists of γ-dendrites and β-precipitated particles. It has been observed that the precipitation and growth of the latter occur along the γ dendrite (Figure 10a–c). In Figure 10c, the precipitates forming in front of the cellular columns can be clearly seen. The presence of the precipitates not only prevents the growth of the cellular columns (indicated as "S"), but in addition, if they are coarse, they also affect the direction of the growth of these with respect to their original orientation (indicated as "C"). Furthermore, in the TEM image in Figure 10d, four parallel strips of bamboo-shaped structure can be observed. This structure basically consists of rod-shaped particles having different lengths. Intervals between these strips were measured and appear to be in the range of approximately 800–1200 nm. Figure 10e shows the electrobeam diffraction pattern performed on the bamboo-shaped dendrite for the NiCoCrAlYTa ESD coating. It was observed that the bamboo-shaped dendrite exhibits the characteristics of β (i.e., a BCC crystalline phase). The high-magnification TEM images clearly highlight the existence of the nanoparticles between two bamboo-like dendrites (Figure 10f,g). These nanoparticles have been identified as a BCC structure, or β phase (Figure 10h). Furthermore, in Figure 10g, it can be observed that the γ phase has a homogeneous cellular substructure of approximately 6 nm inside which some bright white particles are randomly distributed. The bright white particles can be γ′ phases. Meanwhile, from the diffraction pattern reported in Figure 10i, it was observed that the matrix has an FCC structure, which is a γ phase (zone B in Figure 10f) [79].

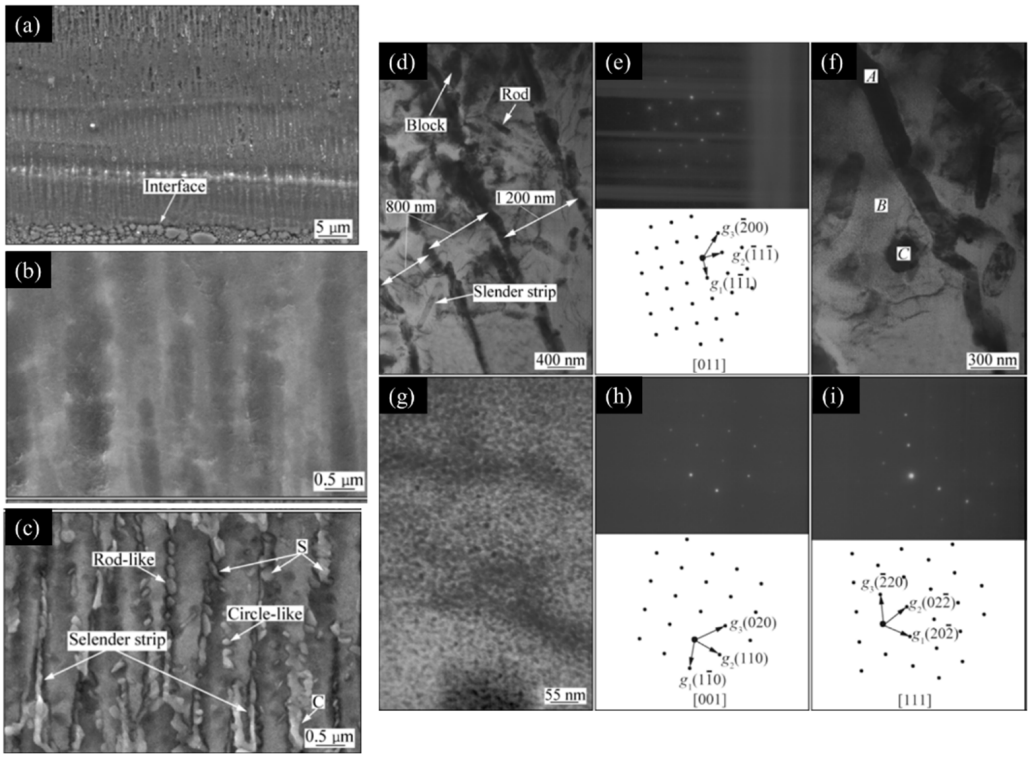

Figure 10. NiCoCrAlYTa ESD built-up coating on the Ni-based DS superalloy (DZ22) blade tip: (**a**) laminate microstructure with a superfine column dendrite, (**b**) few precipitates in the first thin deposited layer, (**c**) distinguished precipitates in the fifth thin deposited layer, (**d**) TEM images showing microstructures of a sublayer near the interface between built-up coating and a substrate: four parallel rows of bamboo-like dendrite, (**e**) electrobeam diffraction pattern from bamboolike dendrite (indicated as A in Figure 10f), (**f**,**g**) magnified images showing nanoparticles existing in inter-dendrites, (**h**) electrobeam diffraction pattern from nanoparticles (indicated as C in Figure 10f), and (**i**) electrobeam diffraction pattern from the matrix (indicated as B in Figure 10f) [79].

In the literature, it has been widely demonstrated that carrying out multiple depositions passes and raising the normalized energy density leads to an increase in the deposit thickness. For example, it has been found for the WE43 alloy deposited upon a homologue substrate, that after 50 subsequent deposition passes, the thickness varies from a minimum of 82.6 µm to a maximum of 407.6 µm obtained at the lowest (0.15 J) and highest spark energy (1.69 J), respectively [51]. However, some authors show that after a given energy value or after a definite pass number, the deposit quality is reduced. In particular, it was found for Al–Ni alloy (Al–3 wt% Ni) that a maximum thickness ranging from ~120 to 140 µm can achieved using a normalized energy density of about 0.689 J/mm^2. At that point, by further increasing the normalized energy density, the thickness does not increase and/or the quality of the coating decreases [77]. According to Johnson et al., this coating thickness limit occurs owing to embrittlement, as a result of induced thermal strain, of the previously deposited layer during subsequent deposition passes [67]. In addition, it has also been found that for the same number of passes and the same level of energy used, the coating thickness changes depending on the metal alloy deposited. Studies report that for several Al alloys, coating thicknesses between 30 and 50 microns are obtained following a single pass using an energy of 0.55 J/pulse [30].

Cao et al. [48] showed for the NiCrAlY coatings deposited on the GH4169 superalloy that different mass gain values were obtained by varying the process parameters (voltage and capacitance). Figure 11 shows the mass gain curves as a function of the number of passes for different values of spark energy *Ep*. The results presented in Figure 11 show that the mass gain, for the same area and the same deposition time, grows linearly as the number of depositions performed increases. More specifically, they observed that mass gain increases more rapidly with increasing voltage, while the opposite trend was found as capacitance increases (i.e., mass gain decreases as capacitance increases). Finally, it was found that high capacitance values generate a less regular splash pattern and a deposit with a greater presence of defects, thus obtaining a lower mass gain value [49,77].

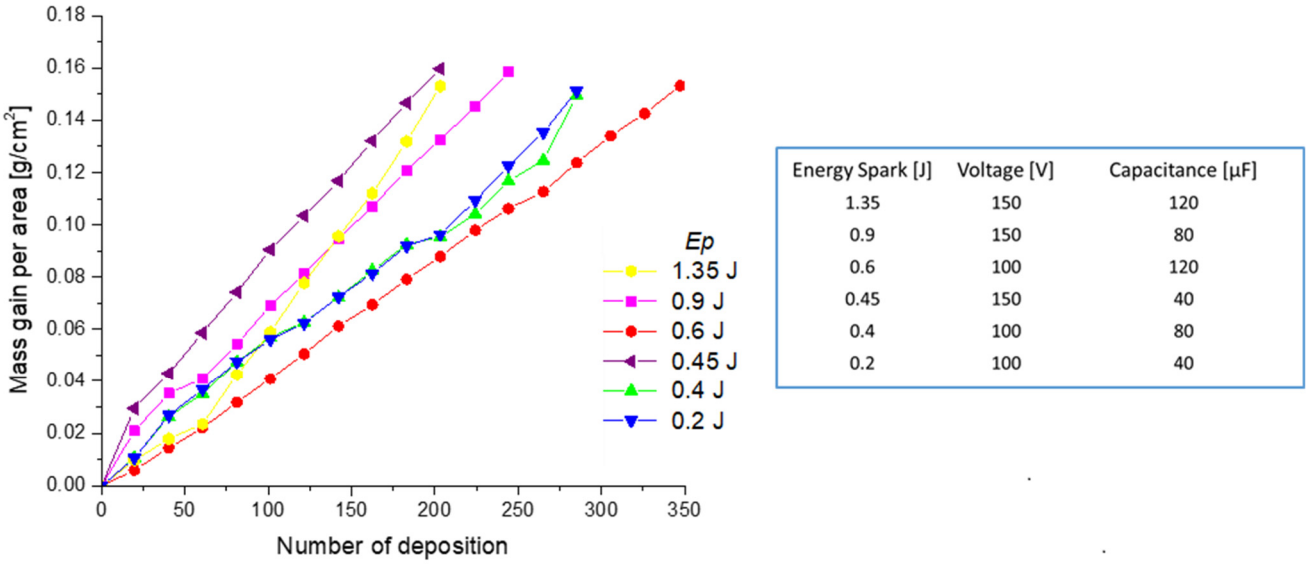

Energy Spark [J]	Voltage [V]	Capacitance [µF]
1.35	150	120
0.9	150	80
0.6	100	120
0.45	150	40
0.4	100	80
0.2	100	40

Figure 11. Mass gain curves of NiCrAlY coatings performed upon a superalloy GH4169 substrate as a function of processing parameters [49].

Similarly, Renna G. et al. [51] reported that the thickness of the deposits varies according to the process parameters used and, consequently, as the spark energy varies. They found that as the spark energy increases, the thickness of the coatings increases. In particular, they showed that thicknesses ranging from 180.4 to 770 µm can be obtained for depositions of A357 alloy electrodes on homologous substrate [50]. The increase in thickness is attributed to a greater quantity of material transferred as the spark energy

increases. At the same time, an increase in the deposit growth rate was also observed. Consequently, an increase in *Ep* leads to shorter deposition times [51,77].

Analysis of Defectiveness of Deposits

Many studies have reported that the shortcomings of electrospark coatings include both a high concentration of defects, such as voids and microcracks, and a high surface roughness. It is well known that the microcracks and voids drastically reduce the resistance of the deposit, while the roughness can represent a real advantage for certain types of application (Figure 12a–c). The typical voids identified within the coating are of three types and are indicated by arrows in Figure 12c: spherical-shaped defects (n°1), random-shaped defects (n° 2), and laminar defects (n° 3). The latter, identified as cracks, can extend through all the deposit both parallel and perpendicular to the substrate/coating interface. It was found that the formation of the first two types of defects (i.e., spherical- and random-shaped defects) depends substantially on the amount of material brought to melting and its distribution [4,20,21,31,51]. Instead, the formation of laminar-shaped defects is mainly due to the thermal stresses generated by the high thermal gradients (G) typical of the electrospark process. More specifically, the cracks that extend perpendicular to the interface are due to the shrinkage that occurs during the solidification and cooling of the deposited material. It was observed that very often these cracks were generated in the very first deposited layers, but they can also originate in subsequent layers and nuclear on the random shape defects present within the deposits [51,80]. In addition, it was found that the perpendicular cracks that were generated in the first deposited layers very often propagate upward through the entire thickness. This is due to the repeated thermal stresses to which the coating is subjected for the entire duration of the construction of the deposit [20,21]. Unlike perpendicular cracks, those that extend instead parallel to the interface are most often generated by poor mixing of the electrode material with the substrate or previously deposited layer and can also originate from the mechanical impact of the electrode during its advancing. These are also known as delamination since they originate at cracks' weakly bonded interfaces [51].

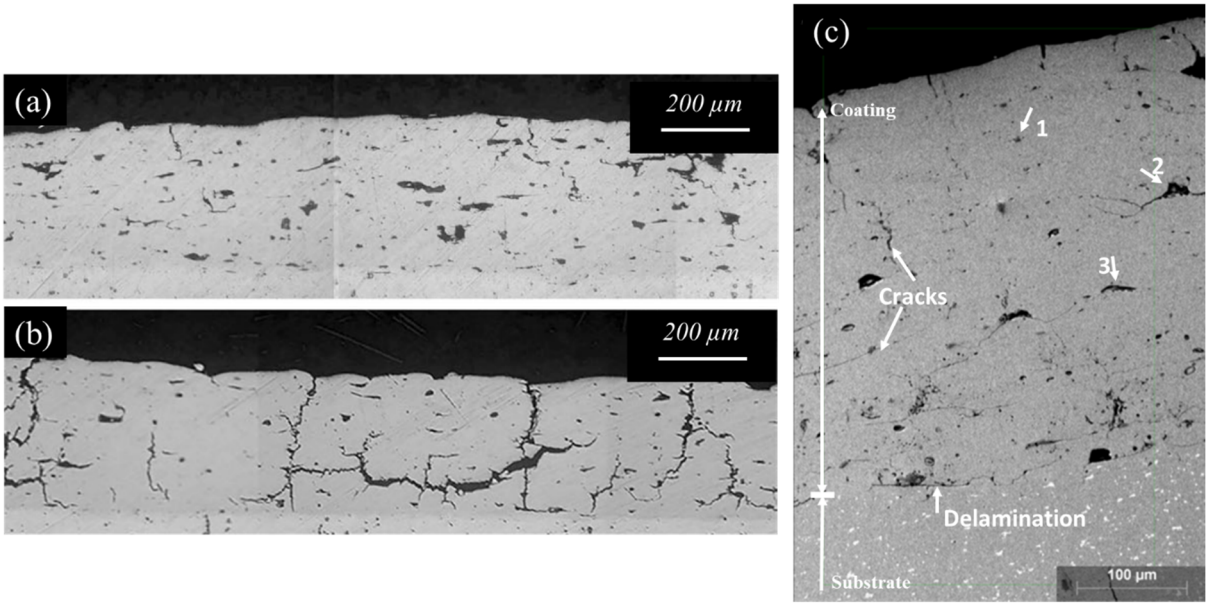

Figure 12. Cross-sectional images of NiCrAlY coatings fabricated on superalloy GH4169 with an Es of (**a**) 0.2 J and (**b**) 1.35 J; as it can be seen, the deposit has some defects [49]. (**c**) SEM micrograph of multiple-layer deposition of 2024-T4 Al alloy coating upon a homologous substrate showing the voids of the ESD deposit (Es = 0.9 J): n° 1 small spherical voids, n° 2 large random-shaped voids, and n° 3 laminar porosity [20].

Researchers found that the defect's density and consequent deposit properties are influenced mainly by the process parameters used. More recently, Leo et al. and coworkers conducted a deep investigation of changes in the defects level in coatings produced with different alloys (i.e., 2024, A357, and WE43 alloy) depending on different process parameters [20,50,51]. In those works, it was noted that there is a general tendency to reduce the percentage area fraction of defects within the coatings as the spark energy (*Ep*) increases. The defectiveness level decreases because when *Ep* increases both the thickness and volume of the splat molten increase, the splat becomes larger [19,20,43].

More specifically, the defect level is reduced because the space between individual splats decreases as the spark energy increases [81]. Furthermore, higher energy values allow to remelting a greater amount of material deposited in the previous pass, reducing or completely eliminating the undulations and surface roughness originated previously [20,82]. In addition, they claimed that, among all process parameters, the percentage of defects in the deposit is most affected by the voltage value (V). Particularly, it has been shown that the percentage of defects within the coatings does not change significantly if the V is kept constant, while if this increases, the percentage of defects is considerably reduced [20,50,51]. Conversely, for the NiCrAlY coatings deposited on superalloy, it was found that the minimum defect density was obtained at low energy levels (100 V and 120 μF; 100 V and 40 μF) [49].

Therefore, since the coating performance depends on the defect density of the coating, it is necessary for each deposited alloy to identify the optimum process parameters that provide effective deposition to achieve the best mechanical properties.

Substrate/Coating Interface Behavior

It is also noteworthy that continuous, adherent, and metallurgical sound substrate/coating interfaces can be commonly achieved with this technique. This metallurgical bonding results in better adhesion between the substrate and the coating than traditional low-energy coating processes, for example, electrochemical plating, detonation gun and plasma spray [42]. Several papers showed that the substrate does not exhibit a heat-affected zone (HAZ) due to the low heat input supplied. Thus, the portion of the base material next to the interface will not exhibit any chemical and microstructural modification. Mixing at the interface among the coating microstructure and the base material was also reported. Figure 11 shows the microstructures near the interface between the substrate and Al–Si coating (Figure 13a–c) and Mg alloy coating (Figure 13d,e). Particularly, near the coating/substrate interface of Al–Si alloy coating, several large Si particles surrounded by a cellular structure are observed (Figure 13a–c) [50]. These Si particles originate from the substrate material and are embedded into the coating by the action of the rotating electrode, which causes the mechanical mixing of the molten material of the substrate with that of the electrode during deposition. Meanwhile eutectic structures embedded in the Mg alloy coating close to the interface (Figure 13b) exhibit a slight dissolution [51].

Some studies on depositing of the thermally sensitive materials, such as 2024 aluminum alloy deposited on a homologue substrate, report some critical changes in the substrate/coating interface. These effects occur in the form of cracks perpendicular to the substrate/coating interface, which extend into the substrate preferentially along the grain boundaries (see Figure 14). As it is known, the AA2024 alloy is susceptible to the formation of solidification cracks and/or liquation cracks during the welding processes, being characterized by large solidification range, high thermal expansion, large solidification shrinkage, and large quantity of alloying addition [20].

Solidification cracking occurs, of course, during the solidification of the melt. It is intergranular, occurring along grain boundaries, and it is due to the shrinkage-induced stresses from both molten metal solidification and nonuniform thermal contraction [20,83,84].

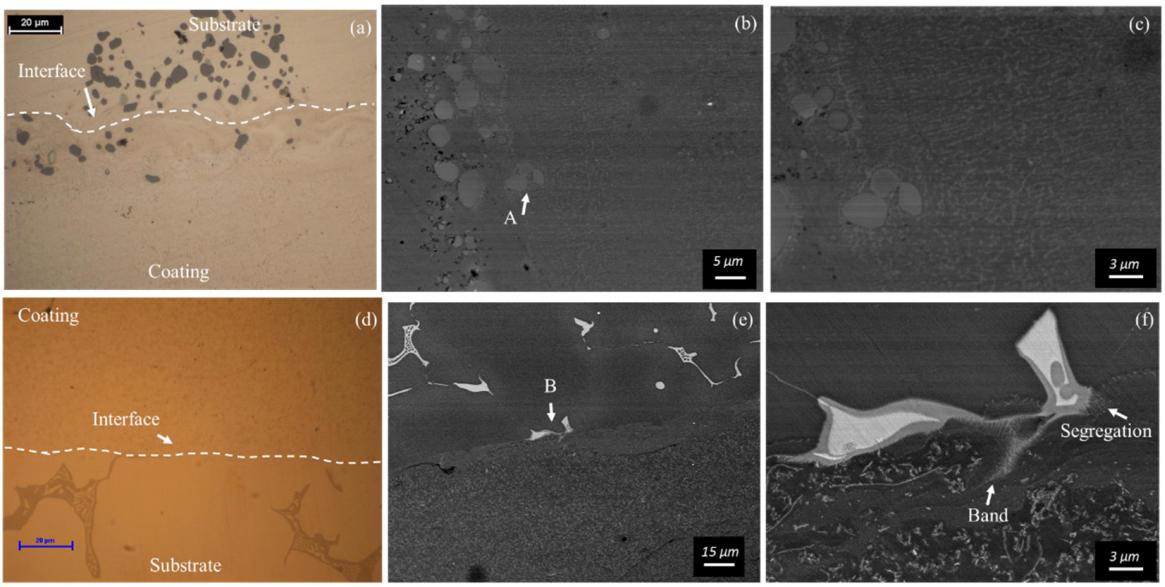

Figure 13. Microstructure close to the substrate/coating interface: (**a**) Optical micrograph and (**b**) scanning electron micrograph of A357-T61 coating deposited upon a homologous substrate [50], (**c**) magnification of the substrate/coating interface (indicated as "A" in Figure 13b, (**d**) OM and (**e**) SEM micrographs of WE43-T6 coating deposited upon a homologous substrate, (**f**) magnification of the substrate/coating interface (indicated as "B" in Figure 13e) [51].

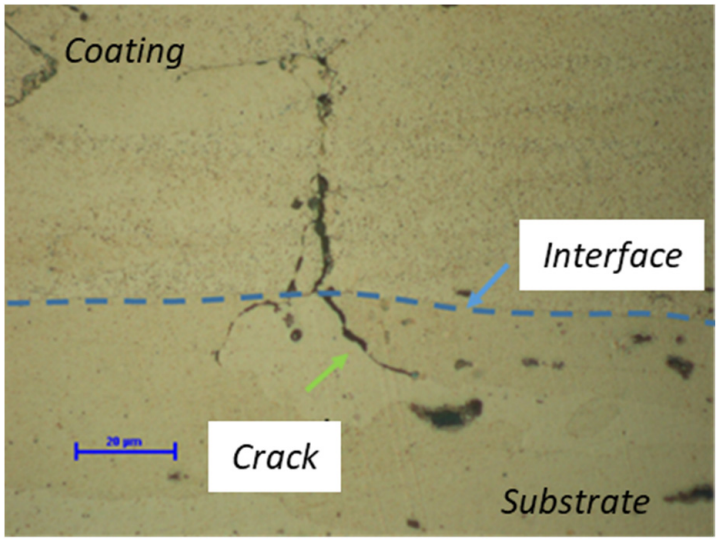

Figure 14. Electrospark deposit in alloy 2024-T4 on a homologous substrate. OM close to the coating/substrate interface showing the cracks that propagate in the base material along the boundary grain.

Liquation cracking occurs at a temperature lower than the solidus temperature during nonequilibrium heating of the alloy, such as in the heat-affected zone of welding, where the peak temperature of the welding cycle is just below the solidus temperature. This liquation cracking is due to the combination of the constitutional liquation phenomenon [84] (localized grain boundaries melting at a temperature significantly below the solidus T of the alloy) and tensile stresses that act on the constitutionally liquated area to produce cracks called liquation cracks.

Studies have shown that, for any setting of the *Ep* level, the process leads to the formation of cracks extending into the substrate along the grain boundaries and that the

average length of these increases with *Ep* (Figure 12). Although the heat input of ESD is lower than that of conventional fusion welding, during the ESD process, the heat input is high enough to melt the substrate, as shown above. Therefore, the temperature of the area close to the coating/substrate interface promotes the melting of some areas where a higher solute concentration develops and locally alters the liquidus (solidus) T of the alloy [20]. At the same time, the rapid cooling due to the electrospark process induces a large thermal strain, which opens the liquated zones [12,85–88].

The presence of these cracks at the interface dramatically reduces the mechanical properties of the base material and, in addition, limits the possibility of carrying out coatings and/or repairs in the 2024 alloy (alloy based on an Al–Cu–Mg system). This alloy was a forerunner of a variety of the 2000 aluminum alloy series. Generally, it is supplied in T4 or T6 conditions, as these heat treatments give higher mechanical properties. It is widely used in the aerospace industry due to its excellent properties, that is, good fracture toughness, excellent resistance to fatigue crack growth, and high strength-to-weight ratio [7,21].

2.7.2. Amorphous Deposits

The major interest in "amorphous metals" (defined as a group of noncrystalline metals) resides in properties that are better than their crystalline counterparts, that is, wear and corrosion resistance and mechanical hardness [40,89,90]. Moreover, the absence of grain boundaries and a homogeneous nature gives amorphous metals unique electronic and magnetic properties. Thanks to their unique properties, these metals have found several applications in industry, such as transformer cores, magnetic storage media, electronic casings, sporting goods, surgical instruments, and corrosion-resistant coatings [91]. An extremely high cooling rate is required to produce amorphous coatings or repair damaged parts without inducing substrate crystallization. In general, the family of zirconium-based alloys (known as Vitreloy), Fe-based alloys, and hard chromium are promising materials for producing protective coatings as they have excellent properties [41,43].

Compared with the traditional techniques (such as laser electron beam surface treatment with gas-atomized powders and magnetron sputtering, vacuum plasma spray, cladding, high-velocity oxygen fuel spray) ESD is a modern technology able to produce amorphous surface layers on substrates made of a thermally sensitive microstructure without destroying their unique properties.

For instance, M. F. Hasanabadi et al. [43] showed that ESD has the ability to produce amorphous layers from Fe-based Fe48Cr18Mo7B16C4Nb7 crystalline alloy on a 316L stainless steel substrate. An important factor considered in this work is the total heat input used for the production of amorphous coatings. In particular, they determined the range of electrical parameters suitable for the production of amorphous alloys. It was found that the coating structure is amorphous at total heat input values lower than 4.4 W, but at values of total heat input above this value (17 and 32 W), the coatings are not completely amorphous. This implies that an increase in the total heat input in this process generates an ultra-fine-grained or nanocrystalline coating structure due to a decrease in the cooling rate [43]. Figure 15a–e shows the FESEM micrographs of the coating cross-section for the sample obtained with a total heat lower (Figure 15a,b) and higher (Figure 15c,d) than 4.4 W. As it can be seen, unlike the sample in Figure 15a, particular phases are formed in the sample obtained with a thermal input of 32 W (Figure 15c). The XRD results show that the crystalline phases formed in this sample are α-Fe and Fe_3B. Based on Figure 15d, the range of precipitate sizes is tens of nanometers to several hundred nanometers. Instead, in Figure 15e, it is possible to identify the boundaries among the fully amorphous region and mixed amorphous/crystalline region of the specimen. Furthermore, it was found that the average hardness of the amorphous coating was found to be about 1300 HV, which is similar to the hardness of amorphous bulk metal (Fe48Cr18Mo7B16C4Nb7 amorphous alloy) [43].

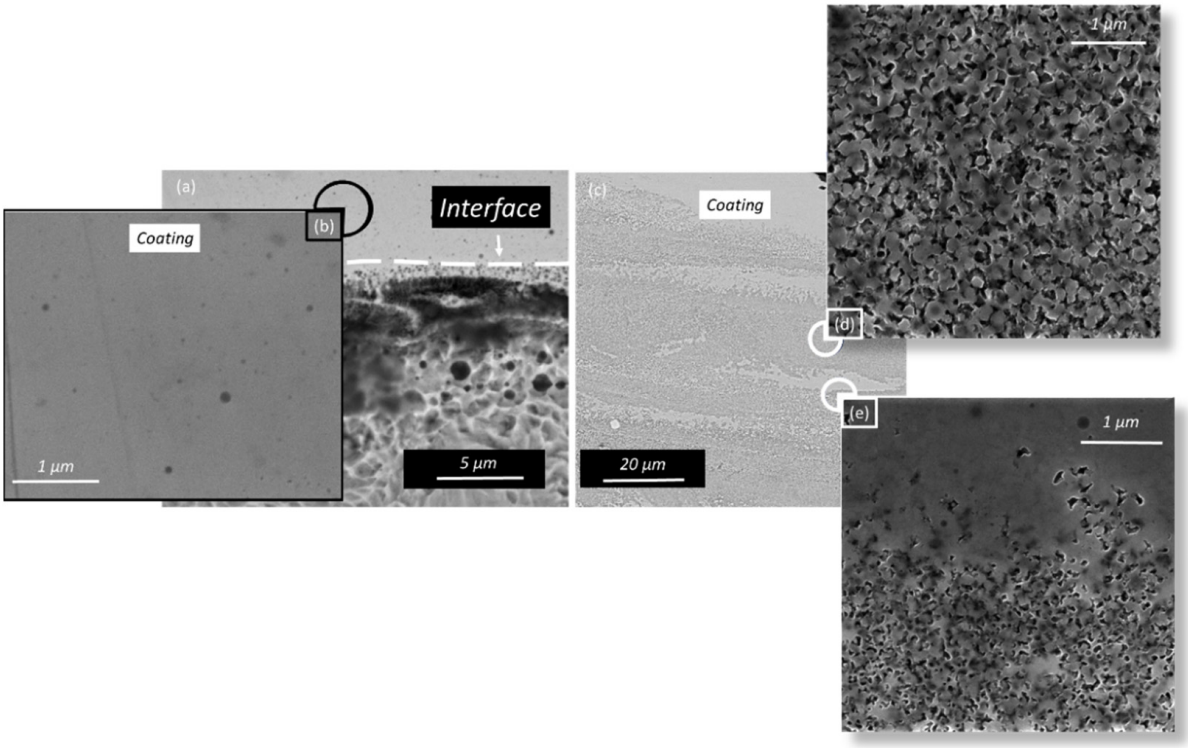

Figure 15. FESEM micrographs for a sample made by depositing an $Fe_{48}Cr_{18}Mo_7B_{16}C_4Nb_7$ crystalline alloy on a 316L stainless steel substrate at: (**a**) 1 W total heat input showing the coating and interface of coating/base metal; (**b**) coating surface with higher magnification. Meanwhile (**c**) FESEM micrographs for a sample at 32 W total heat input etched with an aqua regia agent, (**d**) coating microstructure, (**e**) crystalline phases in coating, and (**c**) amorphous/crystalline interface [43].

S. Cadney and coworkers developed several types of amorphous ESD coatings. In particular, S. Cadney et al. [41] demonstrated that it is possible to deposit an amorphous electrode (Zr41.2Ti13.8Ni10Cu12.5Be22.5) commercially known as Vitreloy on the amorphous substrate without crystallizing the deposit or the substrate. They found that the hardness values of the deposition and substrate were comparable, 508 HV $\pm$ 20 and 514 HV $\pm$ 14, respectively, and no evidence of a heat-affected zone was observed. Similar to what has been observed for nanocrystalline coatings, the thickness of the coating increases with the number of passes for Vitreloy alloy. In another study, S. Cadney et al. [42] deposited Al-based crystalline alloy (Al71.2Co12.2Ce16.6) on the crystalline substrate with a similar composition to the electrode as well as upon to a zirconium-based amorphous substrate (Zr41.2Ti13.8Ni10Cu12.5Be22.5) using the ESD process.

In this work, it is noteworthy that a significant dilution of alloying elements was observed within the deposit, which may result in a weldment composition outside the glass-forming range for the alloy, yielding in either nanocomposites or fully crystalline materials. Moreover, they found that the average weld thickness is 12 $\pm$ 8 μm obtained after 10 passes.

The experimental results obtained from most studies show that the ESD process is unable to create a relevant dilution zone between the base material and the filler metal [24,40,66]. However, most of these studies were conducted as part of repair studies, and thus, combinations of similar materials were used.

A study on the ESD of WC–Co cermets on steel and Ti showed the existence of a dilution zone of about 10 μm, characterized by a chemical composition close to that of the substrate [91]. The observed dilution zone is in line with the results obtained by S. Cadney et al. [42].

Similarly, Liu Dongyan et al. [40] showed the feasibility of obtaining amorphous structure coatings by depositing an Fe-based amorphous electrode (Fe48Cr15Mo14Gd2C15B6) in an amorphous form on a 304 stainless steel crystalline substrate. They found that the coatings are fully dense with a typical thickness of 30 μm. Moreover, they are strongly bonded to the steel substrate and exhibit high microhardness of 1542 kg/mm^2.

2.7.3. Mechanical and Tribological Properties of the Deposits

Typically, the mechanical properties of ESD coatings were evaluated by performing Vickers indentations on the coating cross section. Specifically, some studies, in order to study the effect of a mixed refined microstructure on the hardness values as well as the microstructural characteristic of the built-up coating, were conducted. They performed Vickers indentations at the interfaces between the layers or in line arrangement and perpendicular to the substrate/coating interface. It is well known that the hardness of an alloy is mainly related by the solidification structure. In fact, in full agreement with the Hall–Petch equation, the microhardness value is inversely proportional to the square root of the grain size. Alongside the grain refinement, the hardness of a given alloy can also increase, thanks to the presence of extra fine particles, which are able to increase the activity of the grain boundaries. The latter play a very important role in load transfer in the strengthening of the coating. Additionally, the wear resistance of the coatings is related to the hardness. The tribological performance of an ESD coating depends on the distribution, size, and morphology of the particles present in the deposit as well as the coating thickness [92]. Generally, the main wear mechanisms found are: fatigue wear, adhesive wear, oxidation wear in different conditions, and abrasive wear. Several authors have shown that the hardness of the deposits was generally higher than that of the substrate regardless of the depositing parameters. In particular, they reported that the microhardness of the coatings gradually decreased from the coating top surface to the substrate [49,92–94]. As shown above, the higher hardness value of the ESD coatings compared with that of the substrate is mainly due to the formation of the fine microstructure induced by rapid solidification. For example, W. Wang et al. [93] found that the highest microhardness value of the Mo coating was 1369.5 $HV_{0.1}$, which is about 6.7 times higher than that of the H13 steel substrate, and the wear resistance of the coating was about seven times higher than that of the substrate. The good wear resistance of the coating corresponds to the defect-free and high microhardness of the coating and the good metallurgical bonding between the substrate and coating. Furthermore, the presence of a large number of cemented carbides dispersed in the coating greatly improves the wear resistance of the coating. Similarly, J. S. Wang et al. [92] found a microhardness value of WC-0.8Co coating much higher (1441 $\pm$ 132 $HV_{0.3}$) than the microhardness value of the substrate (320 $\pm$ 10 HV). In addition, they showed that the coating has a good wear resistance, and the average wear resistance was 3.3 times larger than that of the cast steel roll substrate. The high hardness and wear resistance of the coating is determined by the dispersion of fine hard phases in the coating.

Although the fine microstructure present in all coatings confers a greater hardness, in some cases, an average hardness value of the coating equal to [79] or lower than that of the substrate has been observed [20,21,50,51]. In the latter case, the hardness value of the coating is strongly influenced by the presence of widespread defects.

2.7.4. Innovations in Electrospark Deposition

To overcome the shortcomings of the ESD technology, researchers suggest using some effective approaches to improve the quality of deposition, such as applying a magnetic or ultrasound field during the deposition process and optimizing the deposition process.

For example, Ph. V. Kiryukhantsev-Korneev et al. [95] conducted a comparative study of Ti-C-Ni-Fe, Ti-C-Ni-Al and of bilayer Ti-C-Ni-Al/Ti-C-Ni-Fe deposits performed by the electrospark technique using TiCNi electrode (ESD coating), magnetron sputtering of the TiCNiAl target (MS coating), and a combined MS/ESD process. Results showed that the utilization of a combined two-step MS–ESD technology permits us to obtain bilayers made

of Ti-C-Ni-Al/Ti-C-Ni-Fe coatings with improved crack, wear, and oxidation resistance compared with their single-layered Ti-C-Ni-Al counterparts deposited by MS, and with the reduced friction coefficient and enhanced corrosion resistance compared with ESD Ti-C-Ni-Fe coatings. More recently, Ph. V. Kiryukhantsev-Korneev and co-workers [96] showed that the problem of defectiveness of electrospark coatings can be solved by vacuum electrospark alloying deposition (VESA) or even by using a combined VESA–PCAE–MS technology (pulsed cathodic arc evaporation (PCAE) and magnetron sputtering (MS) techniques). Besides, they presented evidence that this latter hybrid technology allows the modification of the structure and the improvement of the protective properties of electrospark coatings, also leading to an increase in corrosion and oxidation resistance at least by 1.5 times in comparison with the VESA coating. Additionally, K. A. Kuptsov et al. [97] showed the advantages of ESD in a vacuum in combination with pulsed arc evaporation (PAE) by depositing WC/a-C coatings on CP-Ti substrate. The main difference between vacuum and air deposition is that, in addition to spark discharges, arc evaporation occurs.

Meanwhile, Yang Liu et al. [98] explored the feasibility of the fabrication of Ti–Al intermetallic compound coatings on Ti–6Al–4V alloy by combined UIT and ESD. Their results demonstrate that UIET (ultrasonic impact electrospark treatment) induces a compressive stress state in the sample. Therefore, UIET is useful for improving the wear, fatigue, and stress corrosion resistance of coatings.

2.8. ESD for Component Repair

Nowadays, applications for advanced materials, such as amorphous or bulk nanocrystalline, are continuously increasing in the aerospace and energy industries. However, despite their enhanced properties, wear and surface damage of components made of these materials continue to occur throughout their service life. Weld repair is nothing more than applying the material to a worn or damaged surface to obtain the original dimensions of the part [99]. Generally, before proceeding with the repair, it is necessary to remove the damaged part by milling or grinding and then rebuilding the missing volume by welding with a suitable filler metal [99,100]. It is known that the microstructure morphology of the substrate and properties of the repaired components are still changed under the influence of the thermal cycle induced by conventional welding [101]. Consequently, the successful implementation of these materials in new, demanding applications depends on the development of low-cost and innovative repair techniques where the novel features of the microstructure can be maintained.

Based on this, many scholars have envisioned that the ESD technique could be used for the repair of worn parts in amorphous or heat-sensitive advanced materials. Most applications and studies focus on high-cost components, for which there are no other low-cost or high-quality technologies.

For this reason, the ESD application, as a repair technology, is of great interest for aerospace and energy industries, in which much high-cost and high-performance materials are subjected to severe operating conditions. Examples of ESD in aerospace applications include repair of diffusion coatings, repair of thermal fatigue cracks in single crystal turbine blades, repair of casting defects, buildup and repair of worn or undersized components, and preplacement of braze alloys on nonweldable superalloys for the precision assembly of components. The use of ESD to repair microcracks or restore damaged surfaces of components involves material deposit thicknesses that are considerably higher than those used for coating and, therefore, deposit characteristics that are performing from all points of view. Studies show that with an increasing deposit thickness, there are increasingly complex microstructural conditions; in particular, the results show a diversification in the microstructure morphology along the thickness [23].

Johnson showed the possibility of repairing a single-crystal turbine blade using ESD. The free-form distortion and low net heat input are just two of the main requirements for the repair of single-crystal alloy components [102]. Figure 16 shows the three steps performed for the repair of the single-crystal turbine blade using the electrospark deposition

technique [102]. Farhat et al. [34] also demonstrated that this technique can be applied to further extend the life of coatings. In particular, they showed that ESD can be successfully used to repair a locally damaged NiCoCrAlY or CoNiCrAlY coating [34].

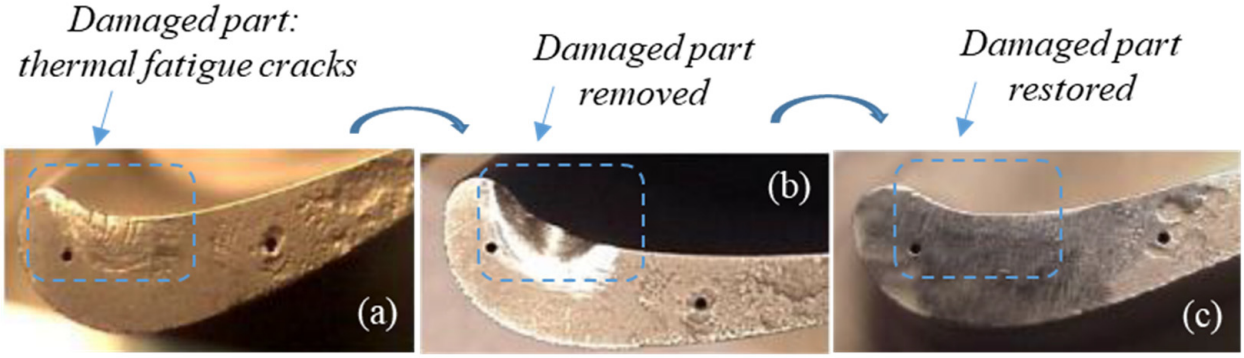

Figure 16. Repair of a turbine blade in single-crystal alloy using the ESD technique: (**a**) image of an as-received turbine blade showing the damaged area characterized by the presence of thermal fatigue cracks, (**b**) removal by grinding of the damaged part from the blade, and (**c**) restoration of the damaged part by depositing homologous material to the substrate [102].

A recent paper [21] shows the results of a comparative study between the repair of AA2024 alloy substrates provided in both T6 (artificial aged) and T4 (natural aged) conditions. The composition of 2024 aluminum alloy includes 3.8%–4.9% Cu and 1.2%–1.8% Mg as major alloying elements. The higher nominal Cu content of 1.5% increases the weld crack sensitivity in AA2024, which, therefore, hinders its weldability. It also has <0.5% Fe, <0.5% Cr, <0.5% Si, <0.25% Zi, <0.15% Ti, and 0.3 | %–0.9% of Mn. The content of other trace in the alloy is less than 0.15%. The repairing of defects was performed with *Ep* equal to 0.9 J. Figure 17 shows the cross-section macrograph and the optical and scanning electron micrographs of the repaired sample. The results showed the same microstructure of the repaired area and the widespread defects as those obtained in the AA2024 coatings [20]; the authors pointed out that the percentage of defects inside the deposit was 2.5%, therefore considered acceptable. In addition, the tensile properties of the repaired specimens (both T6 and T4 states) were found to be lower than the notched ones owing to the residual stresses and the presence of defects. One important factor to take into consideration in such work is the post-repair heat treatment, which improved the yield strength of the repaired specimen by reducing residual stresses. In particular, the authors showed that post-repair heat treatment at 190 °C was most effective when carried out on 2024-T4 since, in addition to a residual stress reduction, the heat treatment also led to a rise in the substrate hardness.

Some studies on the electrospark repair of Ni-based superalloy materials have found favorable deposition properties concerning the substrate material and traditional repair techniques [103]. The experimental results obtained from the tensile and wear tests of the repaired Inconel 718 substrates showed values similar to those of the base material of the ultimate strength, yield strength, and wear rate, although reductions in ductility were observed during the tensile tests [61]. Similar observations were also reported for other Ni-based alloys. A study comparing microplasma and ESD repair processes for Waspaloy showed that the ESD technology achieves greater ultimate strength at the expense of a significant reduction in ductility [104]. In this study, the yield and ultimate strengths achieved for the electrospark-repaired samples were about −2% and −9%, respectively, compared with the base metal samples.

More recently, P. D. Enrique [105] conducted a comprehensive investigation on the mechanical properties of the repaired Inconel 718 samples in relation to microstructure as a function of the set process parameters. The authors presented strong evidence of the effect of microstructure on the fracture toughness and yield strength of repaired ESD samples. In particular, they showed that subgrain microstructure size and the ESD splat boundaries are related to yield strength recovery and that the latter exhibit lower fracture toughness

comparison with the material inside the splat. In other words, an increase in yield strength is obtained as the number of splat boundaries increases since they would act as barriers to the movement of dislocations.

Table 2 shows the tensile property results of the several Al-based and Ni-based substrates repaired by ESD.

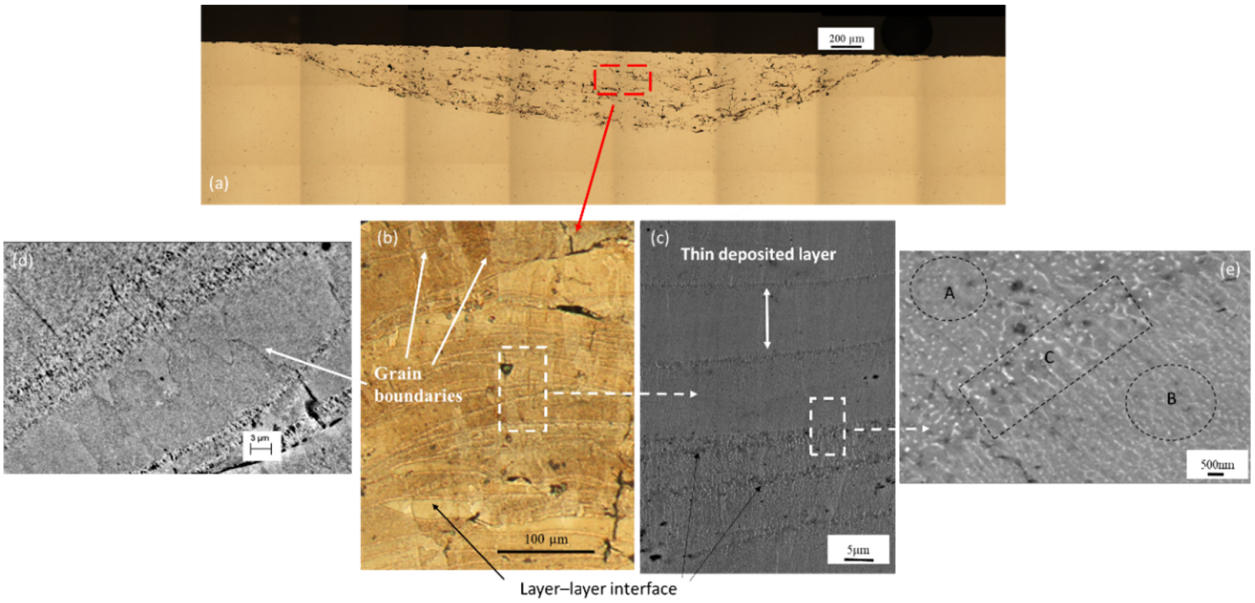

Figure 17. Optical and scanning electron micrograph of a microstructure parallel to the building direction: (**a**) cross-section macrograph of ESD deposit in AA2024-T4 on a homologous substrate; (**b**,**c**) several overlapping layers (morphology cross section); (**d**) long, slender columnar-like grains and within of the layers; and (**e**) fine microstructure to layer–layer interface due to the high cooling rate showing some layers characterized by a cellular dendritic microstructure (pointed by the circle B) and some other layers characterized by uniform distribution of fine small second-phase particles (appearing as light point in circle A). In addition, the layer–layer interface exhibited a coarse microstructure, generally equiaxed (pointed by box C) [21].

Table 2. Summary of tensile properties results for repaired samples using ESD. (PRHT = post-repair heat treatment).

Material	Specimen Type	*Ep* (J)	Yield Strength	Var. %	Ultimate Strength	Var. %	Ref.
AA2024-T4	Base material	0.9	339 MPa		485 MPa		[21]
	Repaired		257 MPa	−24.2	402 MPa	−17	
	Repaired +PRHT_$T_{135°C}$		291MPa	−14.2	419 MPa	−13.6	
	Repaired +PRHT_$T_{190°C}$		329.3 MPa	2.9	442.5 MPa	−8.8	
AA2024-T6	Base material	0.9	482 MPa		516 MPa		[21]
	Repaired		372 MPa	−22.8	439 MPa	−14.9	
	Repaired +PRHT_$T_{135°C}$		411 MPa	−14.	455 MPa	−11.8	
	Repaired +PRHT_$T_{190°C}$		418.8 MPa	−13	457.3 MPa	−11.4	
Waspalloy	Base Material	-	0.617		1000		[104]
	Repaired		0.606	−1.73	0.909	−9.08	
Inconel 718	Base material	0.1	605 MPa		853 MPa		[105]
	Repaired		586 MPa	−3	777 MPa	−9	
	Repaired	0.4	632 MPa	−5	791 MPa	−7	

3. Conclusions

The ESD technology has been exploited for years for the sole purpose of producing coatings on tools and mechanical components subjected to strong thermal and dynamic stresses. The deposition of films with improved properties in terms of hardness, wear resistance and corrosion resistance has therefore allowed for improving the surface properties without modifying the component properties. Over the past few decades, there has been increasing acceptance of the idea of using ESD to extend the service life of mechanical components because of the technological simplicity that distinguishes it from other fusion welding processes, combined with the ability to use it in the shop or in the field. This technology is therefore very interesting for the repair in many applications. In fact, nowadays, the ESD technique is a candidate to an implementation at the industrial scale aimed at repairing superficial damage on aircraft components caused by wear, corrosion, or manufacturing defects. It has been shown that the ESD process is able to form a good metallurgical bond between a substrate and coating without inducing substantial microstructural changes in heat-sensitive substrates (HAZ) and nanocrystalline or amorphous deposits. Moreover, this technique has proved to be suitable for both the fabrication of a wide variety of cermet and metallurgical coatings and the repair of materials, for example superalloys, MCrAlY and thermally sensitive materials (2000 series Al alloy). Irrespective of the process parameters, the deposits show a layer-by-layer microstructure. A cellular columnar structure prevails within the layers, while an equiaxed structure occupies most of the layer–layer interface. Furthermore, the cell size is not uniform across the coating due to the different solidification conditions induced by the process. Anyway, the scale of the microstructure is, in general, quite fine because each splat, when it comes into contact with the substrate, undergoes a rapid solidification process, thanks to the high cooling rates. However, with regard to the thermally sensitive materials, the deposits are affected by several discontinuities that occur as voids and cracks. The formation of voids depends mainly on the amount of material melted during the deposition process and on its distribution. Instead, cracks in general, originate from thermal stresses and from the mechanical impact of the tip of the rotating electrode on the piece during its advancement along the substrate. Very often, cracks nucleate in the first deposited layers and/or on the voids with random morphology present inside the coating.

To improve the performance of deposits, researchers have adopted some effective processes and methods, such as magnetic or ultrasound treatments during the deposition process and post-weld treatment techniques. Although studies have made great achievements, the deposit performance remains lower than that of the substrate, and thus, there is room for improvement. Therefore, it is necessary to carry out further study for the thermally sensitive materials of aeronautical interest as follows: to investigate interactions between parameters of the ESD coating process and their effects on the quality of the deposit. Through this, the process can be optimized for productivity and performance in the application of both coatings and repair.

Author Contributions: Data curation, G.R.; writing—original draft preparation, G.R.; writing—review and editing, C.B., G.P. and G.R.; conceptualization, G.P., C.B. and G.R.; visualization, C.C., G.P. and C.B.; supervision, Catrina Casavola. All authors have read and agreed to the published version of the manuscript.

Funding: This research received no external funding.

Institutional Review Board Statement: Not applicable.

Informed Consent Statement: Not applicable.

Data Availability Statement: Not applicable.

Conflicts of Interest: The authors declare that they have no conflict of interest.

References

1. Paydas, H.; Mertens, A.; Carrus, R.; Lecomte-Beckers, J.; Tchuindjang, T. Laser cladding as repair technology for Ti–6Al–4V alloy: Influence of building strategy on microstructure and hardness. *Mater. Des.* **2015**, *85*, 497–510. [CrossRef]
2. Felix, L.M.; Kwan, C.C.; Zhou, N.Y. The E ect of Pulse Energy on the Defects and Microstructure of Electro-Spark-Deposited Inconel 718. *Metall. Mater. Trans. A* **2019**, *50*, 4223–4231. [CrossRef]
3. Brandt, M. *Laser Additive Manufacturing: Materials, Design, Technologies, and Applications*; Woodhead Publishing: Cambridge, UK, 2016.
4. Verbitchi, V.; Ciuca, C.; Cojocaru, R. Electro-Spark Coating with Special Materials. *Nonconv. Technol. Rev.* **2011**, *1*, 57–62.
5. Vuoristo, P.; Tuominen, J.; Nurminen, J. Laser coating and thermal spraying-process basics and coating properies. In Proceedings of the International Thermal Spray Conference, Basel, Swizerland, 2–4 May 2005.
6. Onjukka, R. Welding vs. *Riveting—Which Has Fatigue Life Airplanes. Weld. J.* **1996**, *75*, 29–33.
7. Davis, J.R. *ASM Specialty Handbook: Aluminum and Aluminum Alloy*; ASM International: Almere, The Netherlands, 1993.
8. Kou, S. *Welding Metallurgy and Weldability of High Strength Aluminum Alloys*; Welding Research Council Bulletin: Madison, WI, USA, 1986.
9. Nogi, K.; Aoki, Y. Behavior of bubbles in welding for repairs in space. *Mater. Des.* **1997**, *18*, 275–278. [CrossRef]
10. Norman, A.F.; Drazhner, V.; Prangnell, P.B. Effect of welding parameters on the solidification microstructure of autogenous TIG welds in an Al-Cu-Mg-Mn alloy. *Mater. Sci. Eng. A* **1999**, *259*, 53–64. [CrossRef]
11. Oates, W.R. *Materials and Applications*, 8th ed.; AWS: Miami, FL, USA, 1972; pp. 1–28.
12. Zhao, H.; White, D.R.; DebRoy, T. Current issues and problems in laser welding of automotive aluminium alloys. *Int. Mater. Rev.* **1999**, *44*, 238–266. [CrossRef]
13. Cao, X.; Wallace, W.; Immarigeon, J.P.; Poon, C. Research and Progress in Laser Welding of Wrought Aluminum Alloys. II. Metallurgical Microstructures, Defects, and Mechanical Properties. *Mater. Manuf. Process.* **2003**, *18*, 23–49. [CrossRef]
14. Feldshteina, E.E.; Kardapolova, M.K.; Gaida, R.; Khorodyski, B.; Kaval'chuk, O.V. Tribological Properties of Electrospark Deposited and Further Laser Hardened Coatings. *J. Frict. Wear* **2013**, *34*, 137–141. [CrossRef]
15. Renna, G.; Leo, P.; Cerri, E.; Zanon, G.P. Thermal shock behaviour of CoCrAlTaY coatings on a Ni-base superalloy. *Metall. Ital.* **2015**, *7–8*, 33–41.
16. Mao, Y.; Li, Z.; Feng, K.; Guo, X.; Zhou, Z.; Wu, Y. Corrosion behavior of carbon film coated magnesium alloy with electroless plating nickel interlayer. *J. Mater. Process. Technol.* **2015**, *219*, 42–47. [CrossRef]
17. Ermakova, E.N.; Sysoev, S.V.; Nikulina, L.D.; Tsyrendorzhieva, I.P.; Rakhlin, V.I.; Kosinova, M.L. Synthesis and characterization of organosilicon compounds as novel precursors for CVD processes. *Thermochim. Acta* **2015**, *622*, 2–8. [CrossRef]
18. Xiang, H.; Ke, F.; Tan, Y.F.; Wang, X.L.; Hua, T. Effects of process parameters on microstructure and wear resistance of TiN coatings deposited on TC11 titanium alloy by electrospark deposition. *Trans. Nonferrous Met. Soc. China* **2017**, *27*, 1767–1776.
19. Tang, S.K. *The Process Fundamentals and Parameters of Electro-spark Deposition*; Master's Thesis, University of Waterloo: Waterloo, ON, Canada, 2009; ISBN1 0494562331. ISBN2 9780494562338.
20. Leo, P.; Renna, G.; Casalino, G. Study of the Direct Metal Deposition of AA2024 by ElectroSpark for Coating and Reparation Scopes. *Appl. Sci.* **2017**, *7*, 945.
21. Renna, G.; Leo, P.; Casalino, G.; Cerri, E. Repairing 2024 Aluminum Alloy via Electrospark Deposition Process: A Feasibility Study. *Adv. Mater. Sci. Eng.* **2018**, *2018*, 8563054. [CrossRef]
22. Xie, Y.J.; Wang, M.C.; Huang, D.W. Comparative study of microstructural characteristics of electrospark and Nd: YAG laser epitaxially growing coatings. *Appl. Surf. Sci.* **2007**, *253*, 6149–6156. [CrossRef]
23. Wang, P.Z.; Pan, G.S.; Zhou, Y.; Qu, J.X.; Shao, H.S. Accelerated Electrospark Deposition and the Wear Behavior of Coatings. *J. Mater. Eng. Perform.* **1997**, *6*, 780–784. [CrossRef]
24. Xie, Y.J.; Wang, M.C. Microstructural morphology of electrospark deposition layer of a high gamma prime superalloy. *Surf. Coat. Technol.* **2006**, *201*, 691–698. [CrossRef]
25. Chen, C.J.; Wang, M.C.; Wang, D.S.; Liu, Y.M. Study on corrosion characteristic of high-energy micro-arc alloying of Al-Y electrode on AZ31 magnesium alloy. *Trans. Mater. Heat Treat.* **2007**, *28*, 106–110. [CrossRef]
26. Frangini, S.; Masci, A. A study on the effect of a dynamic contact force control for improving electrospark coating properties. *Surf. Coat. Technol.* **2010**, *204*, 2613–2623. [CrossRef]
27. Frangini, S.; Masci, A.; di Bartolomeo, A. Cr_7C_3-based cermet coating deposited on stainless steel by electrospark process: Structural characteristics and corrosion behavior. *Surf. Coat. Technol.* **2002**, *149*, 279–286. [CrossRef]
28. Tang, S.K.; Nguyen, T.C.; Zhou, Y. Materials transfer in electro-spark deposition of TiCp/Ni metal-matrix composite coating on Cu substrate. *Weld. Res.* **2010**, *89*, 172–180.
29. Johnson, R.N. Robust coatings for corrosion and wear: The electrospark deposition process. In Proceedings of the Tri-Service Conference on Corrosion, Battelle, Columbus, OH, USA; 1999; pp. 341–410.
30. Brochu, M.; Heard, D.W.; Milligan, J.; Cadney, S. Bulk nanostructure and amorphous metallic components using the electrospark welding process. *Assem. Autom.* **2010**, *30*, 248–256. [CrossRef]
31. Champagne, V.; Pepi, M.; Edwards, B. *Electrospark Deposition for the Repair of Army Main Battle Tank Components*; Army Research Laboratory: Adelphi, MD, USA, 2006.
32. Reynold, J.L.; Holdren, R.L.; Brown, L.E. Electro-Spark Deposition. *Adv. Mater. Process.* **2003**, *161*, 35–37.

33. Wang, W.F.; Wang, M.C.; Sun, F.J.; Zheng, Y.G.; Jiao, J.M. Microstructure and cavitation erosion characteristics of Al–Si alloy coating prepared by electrospark deposition. *Surf. Coat. Technol.* **2008**, *202*, 5116–5121. [CrossRef]
34. Farhat, R. *Repair of Damaged MCrAlY Coatings Targeting Petroleum Industry Applications*; McGill University: Montreal, QC, Canada, 2012.
35. Padgurskas, J.; Kreivaitis, R.; Rukuiža, R.; Mihailov, V.; Agafii, V.; Kriukiene, R.; Baltušnikas, A. Tribological properties of coatings obtained by electro-spark alloying C_{45} steel surfaces. *Surf. Coat. Technol.* **2017**, *311*, 90–97. [CrossRef]
36. Brochu, M.; Portillo, J.G.; Milligan, J.; Head, D.W. Development of Metastable Solidification Structures Using the Electrospark Deposition Process. *Open Surf. Sci. J.* **2011**, *3*, 105–114. [CrossRef]
37. Anisimov, E.; Khan, A.K.; Ojo, O.A. Analysis of Microstructure in Electro-Spark Deposited IN718 Superalloy. *Mater. Charact.* **2016**, *119*, 233–240. [CrossRef]
38. Enrique, P.D.; Jiao, Z.; Zhou, N.Y. Effect of Direct Aging on Heat-Affected Zone and Tensile Properties of Electrospark-Deposited Alloy 718. *Met. Mater. Trans. A* **2019**, *50*, 285–294. [CrossRef]
39. Thamer, A.D.; Hafiz, M.H.; Mahdi, B.S. Mechanism of Building-Up Deposited Layer during Electro-Spark Deposition. *J. Surf. Eng. Mater. Adv. Technol.* **2012**, *2*, 258–263. [CrossRef]
40. Liu, D.Y.; Gao, W.; Li, Z.W.; Zhang, H.F.; Hu, Z.Q. Electro-spark Deposition of Fe-based Amorphous Alloy Coatings. *Mater. Lett.* **2007**, *61*, 165–167. [CrossRef]
41. Cadney, S.; Brochu, M. Formation of amorphous $Zr_{41.2}Ti_{13.8}Ni_{10}Cu_{12.5}Be_{22.5}$ coatings via the electrospark deposition process. *Intermetallics* **2008**, *16*, 518–523. [CrossRef]
42. Cadney, S.; Goodall, G.; Kim, G.; Moran, A.; Brochu, M. The transformation of an Al-based crystalline electrode material to an amorphous deposit via the electrospark welding process. *J. Alloys Compd.* **2009**, *476*, 147–151. [CrossRef]
43. Hasanabadi, F.M.; Ghaini, M.F.; Ebrahimnia, M.; Shahverdi, H.R. Production of amorphous and nanocrystalline iron based coatings by electro-spark deposition process. *Surf. Coat. Technol.* **2015**, *270*, 95–101. [CrossRef]
44. Sheveyko, A.N.; Manakova, O.S.; Zamulaeva, E.I.; Kudryashov, A.E.; Potanin, A.Y.; Sukhorukova, I.V.; Zhitnyak, I.Y.; Gloushankova, N.A.; Levashov, E.A.; Shtansky, D.V. Structural transformations in TiC-CaO-$Ti_3PO_{(x)}$-(Ag_2Ca) electrodes and biocompatible TiCaPCO(N)-(Ag) coatings during pulsed electrospark deposition. *Surf. Coat. Technol.* **2016**, *302*, 327–335. [CrossRef]
45. Petrică, V.; Manuela, C.; Perju, D.-C.A.; Carmen, N. *Advanced Electro-Spark Deposition Process on Metallic Alloys*; IntechOpen: London, UK, 2018; Chapter 3. [CrossRef]
46. Korkmaz, K.; Ribalko, A.V. Effect of pulse shape and energy on the surface roughness and mass transfer in the electrospark coating process. *Kovove Mater.* **2011**, *49*, 265–270. [CrossRef]
47. Changjun, C.; Maocai, W.; Yiming, L.; Dongsheng, W.; Ren, J. Mass transfer trends and the formation of a single deposition spot during high-energy micro-arc alloying of AZ31Mg alloy. *J. Mater. Process. Technol.* **2008**, *198*, 275–280. [CrossRef]
48. Galinov, I.V.; Luban, R.B. Mass transfer trends during electrospark alloying. *Surf. Coat. Technol.* **1996**, *79*, 9–18. [CrossRef]
49. Cao, G.J.; Wang, Y.Y.; Tang, G.Z. Properties of NiCrAlY coatings fabricated on superalloy GH4169 by electrospark deposition. *Int. J. Adv. Manuf. Technol.* **2018**, *96*, 1787–1793. [CrossRef]
50. Leo, P.; Renna, G. *Rivestimenti Via Electrospark Deposition in Lega A357: Microstruttura e Difettosità*; La Metallurgia Italiana: Milano, Italy, 2019.
51. Gilda, R.; Paola, L.; Caterina, C. Effect of ElectroSpark Process Parameters on the WE43 Magnesium Alloy Deposition Quality. *Appl. Sci.* **2019**, *9*, 4383. [CrossRef]
52. Johnson, R.N.; Sheldon, G.L. Advances in the electrospark deposition coating process. *J. Vac. Sci. Technol. A* **1986**, *4*, 2740–2746. [CrossRef]
53. Rawdon, H.S. *Electrospark Deposition for Depot- and Fild-Level Component Repair and Replaced of Heard Chromium Plating*; Final Report; ESTCP: Alexandria, VA, USA, 2006.
54. Welsh, N.C. Frictional Heating and its Influence on the Wear of Steel. *J. Appl. Phys.* **1957**, *28*, 960. [CrossRef]
55. Welsh, N.C. Surface Hardening of Non-ferrous Metals by Spark Discharge. *Nature* **1958**, *181*, 1004. [CrossRef]
56. Welsh, N.C.; Watts, P.E. The wear resistance of spark-hardened surfaces. *Wear* **1962**, *5*, 289–307. [CrossRef]
57. Lazarenko, B.R.; Lazarenko, N.I. *Electric Erosion of Materials*; Gasenergoizdat: Moscow/Leningrad, Russia, 1944.
58. Polyachenko, A.U. *New Methods of Electrical Working of Materials*; Mashgiz: Moscow, Russia, 1955; p. 352.
59. Bunshah, R.F. *Handbook of Deposition Technologies for Films and Coatings*, 2nd ed.; Noyes Publications: Park Ridge, NJ, USA, 1994; pp. 131–163.
60. ASM International. *ASM Handbook—Powder Metal Technologies and Applications*, 10th ed.; ASM Int'l: Materials Park, OH, USA, 1993; p. 978.
61. Sartwell, B.D.; Legg, K.O.; Price, N.; Aylor, D.; Champagne, V.; Pollard, T. *Electrospark Deposition for Depot- and Field-Level Component Repair and Replacement of Hard Chromium Plating*; Final reptort; Naval Research Lab: Washington, DC, USA, 2006.
62. Phillips, A.L. *Welding Handbook*, 6th ed.; Chapter 3; American Welding Society Publisher: Miami, FL, USA, 1968; pp. 20–21.
63. Germer, L.H. Electrical Breakdown between Close Electrodes in Air. *J. Appl. Phys.* **1959**, *30*, 46. [CrossRef]
64. Belik, V.D.; Litvin, R.V.; Koval'chenko, M.S. Effect of pulse duration and size of interelectrode interval on electric-spark spraying. I. Effect of pulse duration and size of interelectrode interval on rate of electric-spark transfer. *Powder Metall. Met. Ceram.* **2006**, *45*, 593. [CrossRef]

65. Bailey, J.A.; Johnson, R.N.; Munley, J.T. Method and apparatus for electrospark deposition. U.S. Patent No. 6,835,908, 28 December 2004.
66. Goto, A.; Akiyoshi, M.; Ochiai, H.; Watanabe, M. Development Of Micro Spark Coating. In Proceedings of the 24th International Congress of The Aeronautical Sciences, Yokohama, Japan, 29 August–3 September 2004.
67. Johnson, R.N. ElectroSpark Deposition: Principles and Applications. In Proceedings of the 45th Annual Technical Conference Proceedings, Society of Vacuum Coaters, Madison, MI, USA, 13–18 April 2002; pp. 87–92.
68. Manuela-Cristina, P.E.R.J.U.; Vizureanu, P.; Nejneru, C. The study of energy transfer on thin layers archieved by electro-spark deposition with TiC electrode. In Proceedings of the International Conference of Scientific Paper, AFASES 2014, Brasov, Romania, 22–24 May 2014.
69. Chan, K.R.; Scotchmer, N.; Zhao, J.; Zhou, Y. *Weldability Improvement Using Coated Electrodes for RSW of HDG Steel*; SAE International: Warrendale, PA, USA, 2006.
70. Liu, J.; Wang, R.; Qian, Y. Formation of a single-pulse electrospark deposition spot. *Surf. Coat. Technol.* **2005**, *200*, 2433–2437. [CrossRef]
71. Lesnjajk, A.; Tusek, J. Processes and properties of deposits in electrospark deposition. *Sci. Technol. Weld. Join.* **2002**, *7*, 391–396. [CrossRef]
72. Kurz, W.; Fisher, D.J. *Fundamentals of Solidification*, 4th ed.; CRC Press: Boca Raton, FL, USA, 1998.
73. Meyers, M.A.; Mishra, A.; Benson, D.J. Mechanical properties of nanocrystalline materials. *Prog. Mater. Sci.* **2006**, *51*, 427–556. [CrossRef]
74. Casellas, D.; Beltran, A.; Prado, J.M.; Larson, A.; Romero, A. Microstructural effects on the dry wear resistance of powder metallurgy Al-Si alloys. *Wear* **2004**, *257*, 730–739. [CrossRef]
75. Slattery, B.E.; Perry, T.; Edrisy, A. Microstructural evolution of a eutectic Al-Si engine subjected to severe running conditions. *Mater. Sci. Eng. A* **2009**, *512*, 76–81. [CrossRef]
76. Shabel, B.S.; Granger, D.A.; Truckner, W.G. Friction and Wear of Aluminum-Silicon Alloys. In *ASM Handbook Friction, Lubrication, and Wear Technology*; ASM International: Materials Park, OH, USA, 1992; pp. 785–794.
77. Heard, D.W.; Brochu, M. Development of a nanostructure microstructure in the Al–Ni system using the electrospark deposition process. *J. Mater. Process. Technol.* **2010**, *210*, 892–898. [CrossRef]
78. Zhang, Z.; Akiyama, E.; Watanabe, Y.; Katada, Y.; Tsuzaki, K. Effect of (alpha)-Al/Al3Ni microstructure on the corrosion behaviour of Al-5.4 wt% Ni alloy fabricated by equal-channel angular pressing. *Corros. Sci.* **2007**, *49*, 2962–2972. [CrossRef]
79. Wang, M.C.; Wang, W.F.; Xie, Y.J.; Zhang, J. Electro-spark epitaxial deposition of NiCoCrAlYTa alloy on directionally solidified nickel-based superalloy. *Trans. Nonferrous Met. Soc. China* **2010**, *20*, 795–802. [CrossRef]
80. Staia, M.H.; Fragiel, A.; Cruz, M.; Carrasquero, E.; Campillo, B.; Perez, R.; Constantino, M.; Sudarshan, T.S. Characterization and wear behavior of pulsed electrode surfacing coatings. *Wear* **2001**, *251*, 1051–1060. [CrossRef]
81. Tušek, J.; Kosec, L.; Lešnjak, A.; Muhič, T. Electrospark Deposition for Die Repair. *Metalurgija* **2012**, *51*, 17–20.
82. Xie, Y.-J.; Wang, M.-C. Epitaxial MCrAlY coating on a Ni-base superalloy produced by electrospark deposition. *Surf. Coat. Technol.* **2006**, *201*, 3564–3570. [CrossRef]
83. Porter David, A.; Easterling, K.E. *Phase Transformations in Metals and Alloys*; Chapman & Hall: London, UK, 1992.
84. Messler, W., Jr. *Principles of Welding*; John Wiley & Sons Inc.: New York, NY, USA, 1999.
85. Ghaini, F.M.; Sheikhi, M.; Torkamany, M.J.; Sabbaghzadeh, J. The relation between liquation and solidification cracks in pulsed laser welding of 2024 aluminium alloy. *Mater. Sci. Eng. A* **2009**, *519*, 167–171. [CrossRef]
86. Metinoz, I.; Cristofolini, I.; Pahl, W.; DeNicolo, A.; Molinari, A. *Studio della Resistenza alla Fatica di Contatto di Acciai Sinterizzati Trattati Termicamente*; La Metallurgia Italiana: Milano, Italy, 2014.
87. Kou, S. *Welding Metallurgy*; John Wiley & Sons: Hoboken, NJ, USA, 2002.
88. Inoue, A.; Takeuchi, A. Recent progress in bulk glassy, nanoquasicrystalline and nanocrystalline alloys. *Mater. Sci. Eng. A* **2004**, *375–377*, 16–30. [CrossRef]
89. Inoue, A.; Shen, B.; Takeuchi, A. Fabrication, properties and applications of bulk glassy alloys in late transition metal-based systems, Mater. *Sci. Eng. A* **2006**, *441*, 18–25. [CrossRef]
90. Salimon, A.I.; Ashby, M.F.; Bre'chet, Y.; Greer, A.L. Bulk metallic glasses: What are they good for? *Mater Sci. Eng.* **2004**, *375*, 385–388. [CrossRef]
91. Ruijun, W.; Yiyu, Q.; Jun, L. Interface behavior study of WC_{92}–Co_8 coating produced by electrospark deposition. *Appl. Surf. Sci.* **2005**, *240*, 42–47. [CrossRef]
92. Wang, J.-S.; Meng, H.-M.; Yu, H.-Y.; Fan, Z.-S.; Su, D.-B. Characterization and wear behavior of WC-0.8Co coating on cast steel rolls by electro-spark deposition. *Int. J. Miner. Metall. Mater.* **2009**, *16*, 707–713. [CrossRef]
93. Wang, W.Q.; Du, M.; Zhang, X.; Luan, C.Q.; Tian, Y.T. Preparation and Properties of Mo Coating on H13 Steel by Electro Spark Deposition Process. *Materials* **2021**, *14*, 3700. [CrossRef]
94. Wang, D.; Gao, J.H.; Zhang, R.; Deng, S.J.; Jiang, S.Y.; Cheng, D.H.; Liu, P.; Xiong, Z.Y.; Wang, W.Q. Effect of TaC particles on the microstructure and oxidation behavior of NiCoCrAlYTa coating prepared by electrospark deposition on single crystal superalloy. *Surf. Coat. Technol.* **2021**, *408*, 126851. [CrossRef]

95. Kiryukhantsev-Korneev, P.V.; Sheveyko, A.N.; Shvindina, N.V.; Levashov, E.A.; Shtansky, D.V. Comparative study of Ti-C-Ni-Al, Ti-C-Ni-Fe, and Ti-C-Ni-Al/Ti-C-Ni-Fe coatings produced by magnetron sputtering, electro-spark deposition, and a combined two-step process. *Ceram. Int.* **2018**, *44*, 7637–7646. [CrossRef]
96. Kiryukhantsev-Korneev, P.V.; Sytchenko, A.D.; Gorshkov, V.A.; Loginov, P.A.; Sheveyko, A.N.; Nozhkina, A.V.; Levashov, E.A. Complex study of protective Cr_3C_2–NiAl coatings deposited by vacuum electro-spark alloying, pulsed cathodic arc evaporation, magnetron sputtering, and hybrid technology. *Ceram. Int.* **2022**, *48*, 10921–10931. [CrossRef]
97. Kuptsov, K.A.; Sheveyko, A.N.; Sidorenko, D.A.; Shtansky, D.V. Electro-spark deposition in vacuum using graphite electrode at different electrode polarities: Peculiarities of microstructure, electrochemical and tribological properties. *Appl. Surf. Sci.* **2021**, *566*, 150722. [CrossRef]
98. Liu, Y.; Wang, D.P.; Deng, C.Y.; Huo, L.X.; Wang, L.J.; Fang, R. Novel method to fabricate Ti–Al intermetallic compound coatings on Ti–6Al–4V alloy by combined ultrasonic impact treatment and electrospark deposition. *J. Alloys Compd.* **2015**, *628*, 208–212. [CrossRef]
99. Thompson, S. *Handbook of Mold, Tool and Die Repair Welding*; Woodhead Publishing: Sawston, UK, 1999.
100. Vedani, M.; Previtali, B.; Vimercati, G.M.; Sanvito, A.; Somaschini, G. Problems in laser repair welding a surface treated tool steel. *Surf. Coat. Technol.* **2007**, *201*, 4518–4525. [CrossRef]
101. Cheng, J.W.; Song, G.; Zhang, X.S.; Liu, C.B.; Liu, L.M. Review of Techniques for Improvement of Softening Behavior of Age-Hardening Aluminum Alloy Welded Joints. *Materials* **2021**, *14*, 5804. [CrossRef]
102. Johnson, R.N. Alternative Coatings for Wear and Corrosion: The Electrospark Deposition Process. In *Proceedings, American Electroplaters and Surface Finishers Society*; Pacific Northwest National Laboratory: Richland, WA, USA, 2002.
103. Chen, C.J.; Wang, M.C.; Wang, D.S.; Liang, H.S.; Feng, P. Characterisations of electrospark deposition Stellite 6 alloy coating on 316L sealed valve used in nuclear power plant. *Mater Sci. Technol.* **2010**, *26*, 276–280. [CrossRef]
104. Carofalo, A.; Dattoma, V.; Nobile, R.; Panella, F.W.; Alfeo, G.; Scialpi, A.; Zanon, G.P. Mechanical Characterization of a Nickel-based Superalloy Repaired using MicroPlasma and ESD Technology. *Procedia Eng.* **2015**, *109*, 312–319. [CrossRef]
105. Enriquea, P.D.; Jiaob, Z.; Zhoua, N.Y.; Toyserkani, E. Effect of Microstructure on Tensile Properties of Electrospark Deposition Repaired Ni-superalloy. *Mater. Sci. Eng. A* **2018**, *729*, 268–275. [CrossRef]